Accepted Manuscript

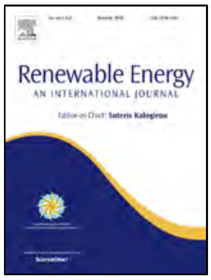

Modeling and dynamic simulation of a steam generation system for a parabolic trough solar power plant

Xiaolei Li, Ershu Xu, Linrui Ma, Shuang Song, Li Xu

PII:	S0960-1481(18)30746-8
DOI:	10.1016/j.renene.2018.06.094
Reference:	RENE 10250
To appear in:	*Renewable Energy*
Received Date:	01 April 2018
Accepted Date:	22 June 2018

Please cite this article as: Xiaolei Li, Ershu Xu, Linrui Ma, Shuang Song, Li Xu, Modeling and dynamic simulation of a steam generation system for a parabolic trough solar power plant, *Renewable Energy* (2018), doi: 10.1016/j.renene.2018.06.094

Modeling and dynamic simulation of a steam generation system for a parabolic trough solar power plant

Xiaolei Li [a,b,c,d], Ershu Xu [a,b,c,d,*], Linrui Ma [a,b,c,d], Shuang Song [a,b,c,d], Li Xu [a,b,c,d]

[a] *Key Laboratory of Solar Thermal Energy and Photovoltaic System of Chinese Academy of Sciences, Beijing, China 100190*

[b] *Institute of Electrical Engineering, Chinese Academy of Sciences, Beijing, China 100190*

[c] *University of Chinese Academy of Sciences, Beijing, China 100049*

[d] *Beijing Engineering Research Center of Solar Thermal Power, Beijing, China 100190*

[*] Corresponding author: xuershu@mail.iee.ac.cn

Abstract

In a parabolic trough solar power plant, the steam generation system is the junction of the heat transfer fluid circuit and the water/steam circuit. Due to the discontinuous nature of solar radiation, the dynamic characteristics of working fluid physical parameters, such as mass flow rate, temperature, and pressure, are more evident in the steam generation system in this kind of plant, increasing the complexity of system operation. In this paper, a zero-dimension dynamic model of an oil/water steam generation system was developed based on the lumped parameter method. Based on the developed model, four typical single-parameter disturbance processes were simulated, and then the control strategy was obtained. System-level simulations on different days (clear and cloudy) and in different seasons (spring, summer, autumn, and winter) were also conducted on a STAR-90 simulation platform using real meteorological data. The simulation results show that PI control can be used to adjust the water level, that system operation on cloudy days should be avoided, and that the system can continue to generate steam after the sun sets. The simulation results can provide a useful reference for plant operators.

Key words

Parabolic trough solar power plant, Steam generation system, System-level simulations, STAR-90

Nomenclature

Latin symbols		V	volume (m^3)
A	heat transfer area (m^2)		
a	volume coefficient 1 (m^3)	*Greek symbols*	
b	volume coefficient 2 (m^3/(kg·s^{-1}))	α	convective heat transfer coefficient (W/(m^2·°C))

c_p	specific heat capacity (J/(kg·°C))	Δ	variation amount
c	mass flow rate coefficient 1 ((kg·s^{-1})/kPa)	λ	resistance coefficient (-)
c'	mass flow rate coefficient 2 ((kg·s^{-1})/MPa)	μ	dynamic viscosity (Pa·s)
d	diameter (m)	ν	kinematic viscosity (m^2/s)
ft	structure correction factor (-)	ρ	density (kg/m^3)
H	level (m)		
h	specific enthalpy (J/kg)	*Subscripts*	
h_{steam}	saturated specific enthalpy of steam (J/kg)	*cond*	condensation
h_q	specific less enthalpy of the feed water (J/kg)	*evap*	evaporation
h_{water}^0	saturated specific enthalpy of water at the previous time step (J/kg)	*f*	fluid
k	thermal conductivity (W/(m·°C))	*i*	inner
l	heat transfer tube length (m)	*in*	inlet
m	mass (kg)	*lam*	laminar
n_t	number of tube-side passes (-)	*o*	outer
Pr	Prandtl number (-)	*out*	outlet
p	pressure (MPa)	*turb*	turbulent
p_1	on-way resistance (Pa)	*w*	wall
p_2	bending resistance (Pa)		
p_3	resistance of the inlet and outlet connecting pipes (Pa)	*Abbreviations*	
Q	heat flow rate (W)	CSP	concentrating solar power
q_m	mass flow rate (kg/s)	DNI	direct normal irradiation
Re	Reynolds number (-)	HTF	heat transfer fluid
r	latent heat of vaporization (J/kg)	HRSG	heat recovery steam generator
S	equivalent bottom area of the evaporator (m^2)	PTSP	parabolic trough solar power
s_1	horizontal tube pitch (m)	SCA	solar collector assembly
s_2	vertical tube pitch (m)	SGS	steam generation system
T	temperature (°C)		
t	time (s)		
u	velocity (m/s)		

1. Introduction

In recent years, the massive use of fossil fuels, including coal, oil, and gas, has led to environmental pollution and energy shortages. It is increasingly important to find alternative fuels. Solar energy has been emphasized by most countries in the world due to its abundance, wide distribution, and low carbon emission. There are many kinds of solar energy utilization technologies, one of which is the concentrating solar power (CSP) technology. CSP technology captures the sun’s direct normal irradiation (DNI), concentrates it onto a receiving surface and transforms the absorbed heat into mechanical work and subsequently electricity, by using state-of-the-art thermodynamic power cycles [1, 2]. The CSP technology is an environmental-friendly renewable energy approach that can greatly contribute to energy conservation and environmental protection [3]. This technology has two advantages, its amenability to hybridization and the ability to readily store energy via thermal energy storage [4]. Therefore, the CSP technology is gradually gaining recognition and acceptance by many countries. According to the International Energy Agency (IEA), the installed capacity of CSP plants will reach 20 GW by 2020 and 800 GW by 2050 [5].

The CSP technology includes four alternatives: parabolic trough solar power, solar power towers, linear Fresnel reflector solar power, and solar dish-Stirling engines. Among them, parabolic trough solar power (PTSP) technology is currently the most commercially mature [1, 6] and the most developed [7, 8]. The benefits of PTSP technology include promising cost-effective investment, mature technology, abundant operational experience, and the ease of coupling with fossil fuels and other renewable energy sources [9].

PTSP plants are mainly composed of collector fields and power blocks. Some PTSP plants are also equipped with thermal energy storage systems and auxiliary fuel systems [10]. The collector field consists of many collectors, each of which is made up of a parabolic trough concentrator and a receiver. The power block includes a steam generation system (SGS), a turbine–generator unit, condenser equipment, and feed-water heat exchangers, such as a deaerator. When the collector field is running, the parabolic trough concentrator gathers the incident sunlight to the receiver fixed at the focal line of the parabolic trough. The heat transfer fluid (HTF) in the receiver absorbs the solar radiation energy, and its temperature increases. Then it releases the absorbed heat to the water in the SGS. The water becomes superheated steam, and it finally drives the steam turbine to complete the power generation process. In general, the HTF in the receiver is thermal oil (a mixture of diphenyl ($C_{12}H_{10}$) and diphenyl oxide ($C_{12}H_{10}O$)) [1], and a study on the use of molten salt (a mixture of 60% $NaNO_3$ and 40% KNO_3 (weight percent)) as an HTF is under way [11]. A typical PTSP plant is shown in Fig. 1.

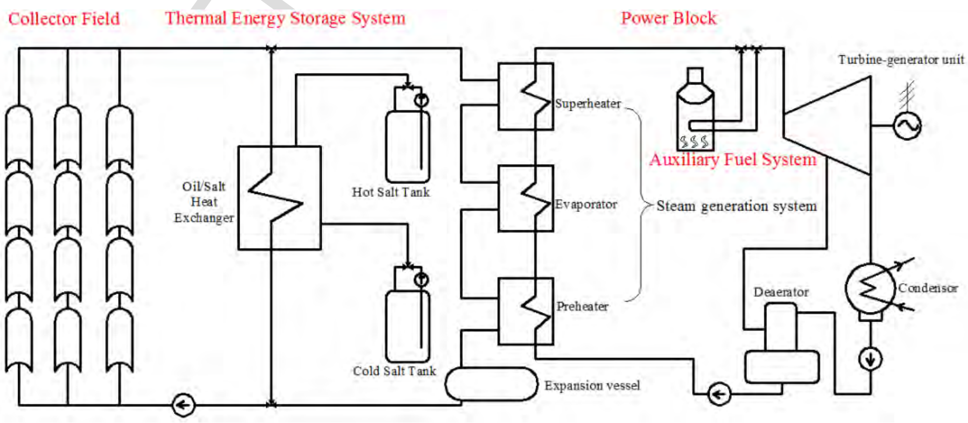

Fig. 1. Schematic diagram of a typical PTSP plant.

As seen in Fig. 1, the SGS is the core equipment of a PTSP plant; it connects the

HTF circuit and the water/steam circuit. It is divided into three parts, namely the preheater, evaporator, and superheater [30]. In the preheater and the superheater, no phase change occurs. In the evaporator, there is a significant phase change process in which the water becomes micro-superheated steam through absorption of heat from the HTF. The function of the SGS is to transfer the heat released by the HTF from the collector field to the feed water in the water/steam circuit and then produce superheated steam with specific parameters to drive the steam turbine. In addition, the SGS isolates the HTF from water/steam.

The SGS is also one of key systems in a conventional thermal power plant, namely, a boiler [12], or in a nuclear power plant [13]. However, since solar radiation, which is the heat source of a solar thermal power plant, is unsteady in comparison with the heat sources of conventional thermal power plants, the focus of research on the SGS of a solar thermal power plant is quite different [14]. For a PTSP plant, the HTF mass flow rate or temperature varies with the sun's DNI, which changes obviously during one day, so the parameters of the steam produced by the SGS also change. As the intersection of the HTF and the water/steam, the SGSs in PTSP plants have more obviously dynamic characteristics in comparison with those in other types of plants, and this increases the complexity of system operation. Hence, it is vital to conduct investigations into the dynamic characteristics of the SGS of a PTSP plant.

Dynamic performance research on SGSs can be pursued by developing a dynamic SGS model. At present, dynamic simulation of SGSs mainly focuses on systems in nuclear power plants or in combined-cycle power plants, namely, heat recovery steam generators (HRSGs). Wang et al. [15] studied the thermo-hydraulic characteristics of an annular tube once-through steam generator in an integrated nuclear power system using the compressible flow model. Zhang et al. [13] built a one-dimensional dynamic mathematical model of the steam generator in the Daya Bay nuclear power plant in China and simulated the dynamic heat transfer performance of the steam generator under varying power. Wan et al. [16] developed the simulation platform of the AP1000 nuclear steam supply system. Sindareh-Esfahani et al. [17, 18] described the dynamic modeling of the HRSG during cold start-up operation in a combined-cycle power plant. Alobaid et al. [19] developed a dynamic model for a subcritical three-pressure-stage HRSG. Mertens et al. [20] simulated warm and hot start-up processes of a drum-type HRSG and a once-through HRSG and studied their different dynamic characteristics. In addition, dynamic simulations of the SGS used for industrial processes were also conducted. Bracco and Cravero [21] studied the variations of the main thermodynamic and physical quantities of a typical small electric steam generator in machines for ironing tasks by developing its mathematical model. Biglia et al. [22] modeled a three-stage steam plant for batch thermal processing of food products, which included a steam boiler, to describe unsteady operative conditions. Allouche et al. [23] conducted dynamic simulation of an integrated solar-driven ejector-based air conditioning system with phase change materials (PCM) cold storage using the Transient System Simulation Program (TRNSYS) software. The steam generator in this system was modelled using the Engineering Equation Solver (EES) software.

In the area of solar energy, simulation research on steam generators began in the

1980s. Ray [24] constructed a nonlinear dynamic model of a once-through subcritical steam generator for solar power tower plants. Ben-Zvi et al. [25] presented an optical and thermal simulation of a new solar tower steam generator, but the developed model was a steady-state model. Pitot et al. [26] analyzed the impact of HRSG characteristics on the performance of a 100-MWe CSP plant with an open volumetric receiver by developing its steady-state model. Terdalkar et al. [27] modeled the Alstom solar receiver steam generator for a tower-type CSP plant using Advanced Process Simulation Software (APROS) and studied its dynamic response under various transient conditions. Henrion et al. [28] conducted a dynamic simulation of an innovative thermal oil-heated SGS designed by Balcke-Duerr for a solar thermal power plant using APROS. The rated operation and the start-up stages of the SGS were simulated. The simulation results revealed a boiling phenomenon in the economizer and a boiling crisis. However, in Henrion's paper, the influence of the variation of DNI on the output of the SGS was not considered. Ponce et al. [29] developed a dynamic simulator for an integrated solar combined-cycle (ISCC) plant in the MATLAB/Simulink environment and presented a model predictive control (MPC) strategy. A dynamic model of a solar steam generator was developed, but DNI disturbance was not considered. El Hefni and Soler [30] developed a dynamic multi-configuration model of a CSP plant with ThermoSysPro library, but the detailed modeling method of the SGS was not presented. Schenk et al. [31] developed a model of an SGS in a PTSP plant with the publicly available ThermoPower library. Nevertheless, the detailed modeling method was not provided in this paper either. Al-Maliki et al. [32, 33] carried out dynamic simulations of an existing 50-MWe parabolic trough solar power plant during clear, slightly cloudy, and very cloudy days using APROS. The plant model includes a steam generator model, but the detailed modeling method was still not given. Some other research has focused on direct steam generation technology. Lobón et al. [34] introduced a computational fluid dynamic simulation approach to predict the behavior of a solar steam-generating system. Suojanen et al. [35] applied a linear Fresnel collector solar field with direct steam generation to generate steam parallel with the steam boiler. Three process configurations for this hybrid plant were modeled using APROS, and the system operation was investigated under varying process conditions. In addition, there has been other research on the safety and economics of SGSs. Pelagotti et al. [36] studied a coil heat exchanger designed by Aalborg specifically for CSP applications as the evaporator of a steam generator. The mathematical model of the coil heat exchanger was developed, and based on this model, stress and fatigue analyses were conducted to optimize the behavior of the system in various start-up scenarios. Rovira et al. [37] compared the annual performance and economic feasibility of an ISCC using two solar concentration technologies: parabolic trough collectors and linear Fresnel reflectors. The ISCC model included a HRSG model that was developed based on the mass and energy balances. González-Gómez et al. [38, 39] presented a thorough economic analysis of the heat exchangers of the steam generator and oil-to-salt heat exchangers of a 50-MWe parabolic trough power plant and conducted thermo-economic optimization of molten salt steam generators in a 110-MWe solar power tower plant. Similar research has been also done by Pizzolato et al. [40]. In addition, Yuan and He et al. [41-43] experimentally studied the thermal performance of thermal oil and molten salt steam generators.

In summary, little literature has referred to the dynamic modeling of SGSs of PTSP plants. Moreover, to the best of our knowledge, there are still two aspects of dynamic SGS simulation that have not been sufficiently addressed in the literature [28-33]. First, the influence of heat source variation, specifically DNI, on the output of the SGS has not been sufficiently considered. Second, a detailed modeling method has not been presented. Previous studies have developed dynamic models of SGSs with specific structures based on existing simulation software, but the details of the modeling methods employed have not been reported. To facilitate dynamic performance research, it is necessary to provide a general modeling method in detail for a certain SGS in a PTSP plant. In this paper, these two aspects are addressed, which is the contribution of this paper.

In this paper, investigations into the dynamic characteristics of an oil/water SGS, the SGS of the Yanqing 1-MWe PTSP pilot plant, were conducted by developing a dynamic simulation model based on the lumped parameter method and certain assumptions. The preheater, evaporator, and superheater models were developed, and together they form the dynamic model of the SGS. Based on the model, four typical single-parameter disturbance processes, namely disturbance of the feed water and the steam mass flow rate as well as step disturbance of the thermal oil inlet mass flow rate and inlet temperature, were simulated. Through an analysis of the simulation results, the control strategy for the system was obtained. Then system-level simulations on different days (clear and cloudy) and in different seasons (spring, summer, autumn, and winter) were conducted on a STAR-90 simulation platform using real meteorological data in Yanqing to analyze the influence of DNI on system parameters. The simulation results provide references for system operation. In addition, in this paper, only the impact of the single factor, DNI, on the SGS was analyzed and other equipment, such as the thermal energy storage system, was not considered.

2. System description

The Yanqing 1-MWe PTSP pilot plant is the first PTSP plant in China, which is located at Yanqing District (latitude 40.38˚ N, longitude 115.94˚ E) in Beijing, capital of China. The plant is supported by the “Research and Demonstration of Parabolic Trough Solar Power Technology” project, which is the key project of the National High Technology Research and Development Program of China (863 Program, which means that it was first launched in March in 1986) during China’s 12th Five-Year Plan. Similar to most other PTSP plants, the Yanqing 1-MWe PTSP pilot plant is mainly made up of a collector field and a power block. The area of the collector field is 10,000 m^2, which includes three 600-m-long loops. One loop has a North–South layout, and the other two loops have East–West layouts [44]. The HTF in the collector field is thermal oil. The PTSP pilot plant is also equipped with a thermal energy storage system, which is different from the traditionally utilized low-cost sensible heat storage in insulated tanks with eutectic mixtures of KNO_3 and $NaNO_3$ molten salts [45]. It is a two-stage thermal energy storage system, including high- and low-temperature subsystems. The thermal energy storage media used in the high-temperature subsystem is thermal oil, and the low-temperature subsystem is a steam accumulator. A schematic diagram and photographs of the Yanqing 1-MWe PTSP pilot plant and its oil/water SGS are shown in Fig. 2 and Fig. 3, respectively.

The rated operation parameters of the SGS are given in Fig. 2. In nominal operation, the mass flow rate of the thermal oil in the collector field is 74,130 kg/h, and its outlet temperature is 393 °C, which is also the inlet temperature of the thermal oil in the SGS. The temperature of the thermal oil decreases to 296 °C after it flows through the SGS. The inlet mass flow rate and the temperature and pressure of the feed water in the SGS are 6,500 kg/h, 104 °C, and 3.21 MPa, respectively. The feed water is first preheated in the preheater. Then it enters the evaporator to become saturated steam after it absorbs heat from the thermal oil, the temperature and pressure of which are 235.1 °C and 3.12 MPa, respectively. The saturated steam is superheated after it flows through the superheater of the SGS, and the outlet temperature and pressure of the superheated steam are 383 °C and 3.1 MPa, respectively.

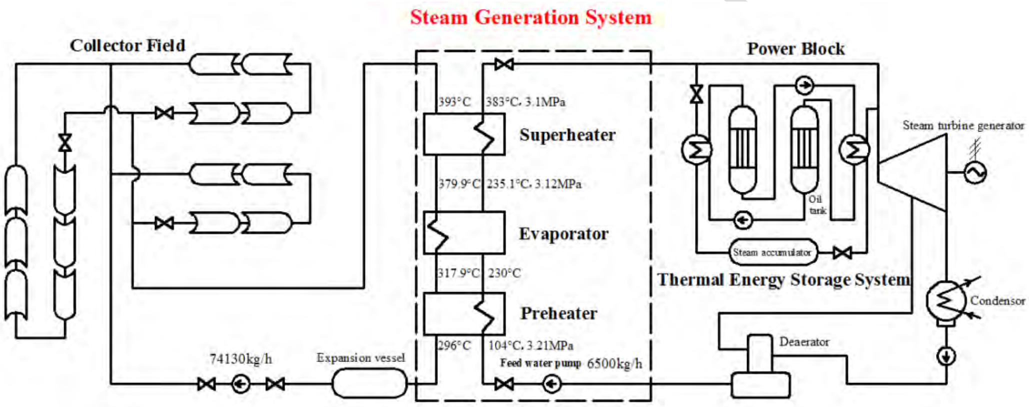

Fig. 2. Schematic diagram of the Yanqing 1-MWe PTSP pilot plant and its SGS.

(a) Yanqing 1-MWe PTSP pilot plant

(b) SGS

Fig. 3. Photographs of Yanqing 1-MWe PTSP pilot plant and its SGS.

3. Methodology

3.1. STAR-90 simulation platform

The SGS of the Yanqing 1-MWe PTSP pilot plant was modeled on the STAR-90 simulation platform, which is an open-source software developed by Baoding Sinosimu Technology Co. Ltd. in China. STAR-90 was at first used for full-scale and real-time dynamic simulations of conventional thermal power plants to guide their operation and production. Now, it is applied in wider fields, such as nuclear power, hydropower, aerospace, and petrochemicals, and it also has been usefully applied in the modeling and simulation of CSP plants [3, 46-49]. STAR-90 is a simulation platform based on modular modeling. Every user can build needed equipment modules on the basis of physical principles, namely mass, momentum, and energy conservation and save C language-based module algorithm in the STAR-90 algorithm library, which supports revision and updating by users. In addition, STAR-90 has the function of user-defined graphic visualization so that model graphs can be designed according to users' preferences. Therefore, this simulation platform has a clear human–machine interface. In this study, a dynamic model of the SGS was developed separately, and then it was connected with models of other equipment already existent in the STAR-90 library, such as valves, pumps, and so forth, to complete the system-level simulations on the STAR-90 simulation platform.

3.2. Dynamic simulation model of the SGS

The modeling method adopted in this paper is the lumped-parameter method. This method treats state parameters of the working medium in a system as homogeneous. It selects state parameters of a representative point in the space as state parameters of the whole system; thus, the lumped-parameter model is a zero-dimension model. The lumped-parameter model can realize real-time simulations because it requires less computational effort than the computational fluid dynamics (CFD) model. In addition, for investigations into the dynamic characteristics of one component at the system level, variations of the working fluid parameter at the outlet are a greater concern. The purpose of the lumped-parameter model is to describe the overall system performance and component interaction rather than to describe the finer details occurring within a system [24]. Therefore, from this point of view, the lumped-parameter model has an advantage over a one-dimension model. A detailed description and specific advantages of the lumped-parameter method can be found in the literature [50].

In this paper, the preheater, the evaporator, and the superheater were modeled separately according to three fundamental conservation laws, namely the law of mass conservation, the law of momentum conservation, and the law of energy conservation. Then the three models were connected on the STAR-90 simulation platform, which means the output parameters of the former component are the input parameters of the latter, to form the SGS dynamic model. A schematic diagram of the model is shown in Fig. 4. In the development of the model, the following assumptions were made:

i. For the preheater and the superheater, the outlet point in the space is selected as the lumped parameter point, which means that the working fluid parameters at the outlet are selected as the lumped parameters.

ii. Only the pressure drop at the steam side in the superheater is considered.

iii. The water and steam in the evaporator are under the same saturation state, and their temperature and pressure change at the same time.

iv. The water and steam in the evaporator are separated completely.

v. The thermal conduction of the wall is ignored, and it only has thermal storage capacity.

vi. The SGS is insulated well, so the heat loss is ignored.

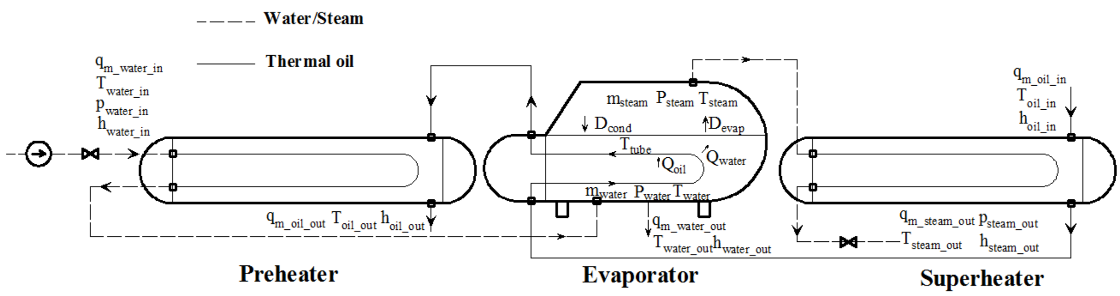

Fig. 4. Schematic diagram of the SGS model.

3.2.1 Thermal oil and water/steam properties

Since thermal oil and water/steam properties vary with their temperature and pressure, they must be considered during simulations. Therminol-VP1 is used as thermal oil and correlations between its properties and temperature are provided in [51], which are listed below (12 °C to 425 °C, T is in °C):

Density (kg/m^3):

$$\rho = -0.90797\times T + 0.00078116\times T^2 - 2.367\times 10^{-6}\times T^3 + 1083.25, \quad (1)$$

Specific heat capacity (J/(kg·°C)):

$$c_p = 2.414\times T + 5.9591\times 10^{-3}\times T^2 - 2.9879\times 10^{-5}\times T^3 + 4.4172\times 10^{-8}\times T^4 + 1498, \quad (2)$$

Thermal conductivity (W/(m·°C)):

$$k = -8.19477\times10^{-5}\times T - 1.92257\times10^{-7}\times T^2 + 2.5034\times10^{-11}\times T^3 - 7.2974\times10^{-15}\times T^4 + 0.137743\,, \quad (3)$$

Kinematic viscosity (m^2/s):

$$\nu = e^{\left(\frac{544.149}{T+114.43}-2.59578\right)}\times10^{-6}\,. \quad (4)$$

The specific enthalpy of thermal oil is also provided in [51].

The IAPWS-IF97 [52] is widely used to calculate water/steam properties, and it is also employed in this paper. The relevant calculation is programmed by C language and the program is used to obtain the values of the water or steam properties during dynamic simulations.

3.2.2 Modeling of the preheater and superheater

Tube and shell heat exchangers were selected as the preheater and the superheater because they have the advantages of easy manufacturing, easy cleaning, and reliable operation. In the preheater, the working fluid at the shell side is thermal oil and that at the tube side is water. In the superheater, the fluid flowing through the shell side is also thermal oil, but the working fluid at the tube side is steam. The design parameters of the preheater and the superheater are shown in Table 1.

TABLE 1. SGS parameters

Design parameters	Preheater	Superheater	Evaporator
Area of heat transfer (m^2)	10	47	40
Number of shell-side passes (-)	1	1	1
Number of tube-side passes (-)	4	4	2
Tube outer diameter (m)	0.016	0.016	0.016
Tube inner diameter (m)	0.012	0.012	0.012
Tube specific heat capacity (J/(kg·K))	529	529	529
Tube density (kg/m^3)	7850	7850	7850
Single tube length (m)	4	4	4
Tube bundle layout (-)	Triangular	Triangular	Triangular
Shell-side effective volume (m^3)	0.26	0.63	1.86
Tube-side effective volume (m^3)	0.063	0.25	0.2
Working fluid at the tube side	Water	Steam	Thermal oil
Working fluid at the shell side	Thermal oil	Thermal oil	Water/Steam

The working fluid in the preheater or superheater undergoes no phase change, so the preheater and superheater are single-phase heat exchangers, and their modeling method is relatively simple. To accomplish the dynamic modeling of the preheater, the thermal oil side, heat transfer tube wall, and preheated water side should be modeled respectively. The modeling method includes the following steps.

The energy conservation equations based on thermodynamics [53] and heat transfer principles [54] at the thermal oil side are expressed as

$$\frac{d(c_{p\_oil} m_{oil} T_{oil})}{dt} = q_{m\_oil}(h_{oil\_in} - h_{oil\_out}) - Q_{oil}\,, \quad (5)$$

$$Q_{oil} = \alpha^{'} A_o (T_{oil} - T_{tube}) . \tag{6}$$

Here, the convective heat transfer coefficient $\alpha^{'}$ is calculated by the Zhukauskas correlations [54]:

$$\begin{aligned}
&\alpha^{'} = 1.04 Re_f^{0.4} Pr_f^{0.36} (\frac{Pr_f}{Pr_w})^{0.25} \frac{k}{d_o} (1 \le Re_f \le 5\times10^2, 0.6 \le Pr \le 500) , \\
&\alpha^{'} = 0.71 Re_f^{0.5} Pr_f^{0.36} (\frac{Pr_f}{Pr_w})^{0.25} \frac{k}{d_o} (5\times10^2 < Re_f \le 10^3, 0.6 \le Pr \le 500) , \\
&\alpha^{'} = 0.35 (\frac{s_1}{s_2})^{0.2} Re_f^{0.6} Pr_f^{0.36} (\frac{Pr_f}{Pr_w})^{0.25} \frac{k}{d_o} (10^3 < Re_f \le 2\times10^5, 0.6 \le Pr \le 500) , \\
&\alpha^{'} = 0.031 (\frac{s_1}{s_2})^{0.2} Re_f^{0.8} Pr_f^{0.36} (\frac{Pr_f}{Pr_w})^{0.25} \frac{k}{d_o} (2\times10^5 < Re_f \le 2\times10^6, 0.6 \le Pr \le 500) .
\end{aligned} \tag{6-a}$$

The energy conservation equations based on thermodynamics and heat transfer principles at the preheated water side are given as

$$\frac{d(c_{p\_water} m_{water} T_{water})}{dt} = q_{m\_water} (h_{water\_in} - h_{water\_out}) + Q_{water} , \tag{7}$$

$$Q_{water} = \alpha A_i (T_{tube} - T_{water}) . \tag{8}$$

Here, the convective heat transfer coefficient α is calculated by the Dittus–Boelter formula [54]:

$$\alpha = 0.023 Re_f^{0.8} Pr_f^{0.4} \frac{k}{d_i} (10^4 < Re_f < 1.2\times10^5, 0.7 < Pr_f < 120, \frac{l}{d_i} \ge 60) \cdot \tag{8-a}$$

The energy conservation equation based on the thermodynamics principle at the heat transfer tube wall is expressed as

$$\frac{d(c_{p\_tube} m_{tube} T_{tube})}{dt} = Q_{oil} - Q_{water} . \tag{9}$$

The modeling method of the superheater is similar to that of the preheater; the only difference is that the working fluid at the tube side is steam, not water. In addition, the pressure drop at the steam side needs to be considered. Pressure drop formula is given in Eq. (10) [55]:

$$\Delta p_{steam} = (ft \cdot (\Delta p_1 + \Delta p_2) + \Delta p_3) \times 10^{-6} , \tag{10}$$

$$\Delta p_2 = 4 \frac{\rho_{steam} u_{steam}^2}{2} n_t , \tag{10-a}$$

$$\Delta p_3 = 1.5 \frac{\rho_{steam} u_{steam}^2}{2} , \tag{10-b}$$

$$\begin{aligned}
&\Delta p_1 = \lambda \frac{l}{d_i} \frac{\rho_{steam} u_{steam}^2}{2} (\frac{\mu}{\mu_w})^{-0.14} (Re_{steam} > 2100) \\
&\Delta p_1 = \lambda \frac{l}{d_i} \frac{\rho_{steam} u_{steam}^2}{2} (\frac{\mu}{\mu_w})^{-0.25} (Re_{steam} < 2100)
\end{aligned} , \tag{10-c}$$

where λ can be obtained by the following formula [25]:

$$\begin{aligned} &\lambda = \lambda_{lam} && (Re_{steam} < 2000)\ , \\ &\lambda = \max\{\lambda_{lam}, \lambda_{turb}\} && (2000 \le Re_{steam} \le 4000)\ , \\ &\lambda = \lambda_{turb} && (Re_{steam} > 4000)\ , \end{aligned} \tag{10-c-1}$$

with

$$\lambda_{lam} = \frac{64}{Re_{steam}}\ , \qquad \lambda_{turb} = (1.82 \lg Re_{steam} - 1.64)^{-2}\ . \tag{10-c-1-1}$$

3.2.3 Modeling of the evaporator

A kettle-type heat exchanger is used as the evaporator of the SGS in Yanqing, which is a kind of heat exchanger for steam generation. The most obvious difference between a kettle-type heat exchanger and a general one is that there is a large space on the upper side of the tube bundle for steam generation. The hot working fluid, namely, thermal oil, flows through the heat transfer tubes and releases heat to the water at the shell side. The water undergoes no phase change until it reaches the saturation point. Then steam starts to appear around the heat transfer tubes and rises. Some water is carried by the rising steam, which is separated by the steam-water separator at the top of the shell. It then flows back along both sides of the shell. A photograph of the evaporator is shown in Fig. 5 and its design parameters are presented in Table 1.

Fig. 5. Photograph of the evaporator.

The modeling of the evaporator is more complex than that of the preheater and superheater because the boiling process occurs, and there is two-phase flow at the shell side [17]. To accomplish the dynamic modeling of the evaporator, the thermal oil side, heat transfer tube wall, and the two-phase flow of the water/steam side should be modeled separately. In addition, the water level in the evaporator should also be modeled because it is an important operation parameter for the SGS. To model the water level, the steam volume at the shell side needs to be divided into two parts, one below the water surface and the other above the water surface. The water dynamic evaporation and the steam dynamic condensation should be considered as well. A schematic diagram of the evaporator model is shown in Fig. 6. The modeling method of the evaporator includes the following steps.

The energy conservation equations based on thermodynamics and heat transfer principles at the thermal oil side are expressed as

$$\frac{d(c_{p\_oil} m_{oil} T_{oil})}{dt} = q_{m\_oil}(h_{oil\_in} - h_{oil\_out}) - Q_{oil}\,, \tag{11}$$

$$Q_{oil} = \alpha A_i (T_{oil} - T_{tube})\,, \tag{12}$$

where the convective heat transfer coefficient α is also calculated by the Dittus–Boelter formula:

$$\alpha = 0.023 Re_f^{0.8} Pr_f^{0.3} \frac{\lambda}{d_i} (10^4 < Re_f < 1.2\times10^5, 0.7 < Pr_f < 120, \frac{l}{d_i} \geq 60)\cdot \tag{12-a}$$

The mass and energy conservation equations based on thermodynamics and heat transfer principles at the water/steam side are expressed as follows:

mass conservation equation:

$$\frac{d(\rho_{water} V_{water} + \rho_{steam} V_{steam})}{dt} = q_{m\_water\_in} - q_{m\_steam\_out} - q_{m\_water\_out}\,, \tag{13}$$

$$V_{water} + V_{steam} = V = const\,, \tag{14}$$

energy conservation equation:

$$\frac{d(\rho_{water} V_{water} h_{water} + \rho_{steam} V_{steam} h_{steam})}{dt} = q_{m\_water\_in} h_{water\_in} - q_{m\_water\_out} h_{water} - q_{m\_steam\_out} h_{steam} + Q_{water}\,, \tag{15}$$

$$Q_{water} = \alpha^{'} A_o (T_{tube} - T_{water})\,. \tag{16}$$

Here, the convective heat transfer coefficient at the water side $\alpha^{'}$ is considered as a constant, and its value is obtained by the steady-state operation condition of the SGS [56].

Equations (13), (14), (15) can be transformed into

$$\frac{d\rho_{water}}{dt} V_{water} + \frac{dV_{water}}{dt} \rho_{water} + \frac{d\rho_{steam}}{dt} V_{steam} + \frac{dV_{steam}}{dt} \rho_{steam} = q_{m\_water\_in} - q_{m\_steam\_out} - q_{m\_water\_out}\,, \tag{13'}$$

$$\frac{dV_{water}}{dt} = -\frac{dV_{steam}}{dt}\,, \tag{14'}$$

$$\begin{aligned}&(\frac{dh_{water}}{dt}\rho_{water}+\frac{d\rho_{water}}{dt}h_{water})V_{water}+(\frac{dh_{steam}}{dt}\rho_{steam}+\frac{d\rho_{steam}}{dt}h_{steam})V_{steam}\\&+\frac{dV_{water}}{dt}\rho_{water}h_{water}+\frac{dV_{steam}}{dt}\rho_{steam}h_{steam}\\&=q_{m\_water\_in}h_{water\_in}-q_{m\_water\_out}h_{water}-q_{m\_steam\_out}h_{steam}+Q_{water}\end{aligned} \quad . \qquad (15')$$

Using equations (13'), (14'), (15') and the relationship $\frac{d}{dt}=\frac{\partial}{\partial p_{steam}}(\frac{dp_{steam}}{dt})$ and eliminating $\frac{dV_{water}}{dt}$ and $\frac{dV_{steam}}{dt}$, the dynamic expression of the steam pressure in the evaporator is derived as

$$\frac{dp_{steam}}{dt}=\frac{Q_{water}+(\frac{r\rho_{steam}}{\rho_{water}-\rho_{steam}}-h_q)q_{m\_water\_in}-\frac{r\rho_{steam}}{\rho_{water}-\rho_{steam}}q_{m\_water\_out}-\frac{r\rho_{water}}{\rho_{water}-\rho_{steam}}q_{m\_steam\_out}}{\left[\rho_{water}\frac{\partial h_{water}}{\partial p_{steam}}+\frac{r\rho_{steam}}{\rho_{water}-\rho_{steam}}(\frac{\partial\rho_{water}}{\partial p_{steam}})\right]V_{water}+\left[\rho_{steam}\frac{\partial h_{steam}}{\partial p_{steam}}+\frac{r\rho_{water}}{\rho_{water}-\rho_{steam}}(\frac{\partial\rho_{steam}}{\partial p_{steam}})\right]V_{steam}} \quad , (17)$$

where r is the latent heat of vaporization, and $r=h_{steam}-h_{water}$. h_q is the lower enthalpy of the feed water, $h_q=h_{water}-h_{water\_in}$.

The variation of the steam pressure in the evaporator can influence the mass flow rate of the working fluid. As a result, the feed water mass flow rate at the inlet and the steam mass flow rate at the outlet are considered as variables, which are calculated according to the following formulae [56]:

$$q_{m\_water\_in}=c\sqrt{p_{water\_in}-p_{steam}} \,, \qquad (18)$$

$$q_{m\_steam\_out}=c'p_{steam} \,, \qquad (19)$$

where c and c' are coefficients of the mass flow rate, which can be obtained by the steady-state operation condition.

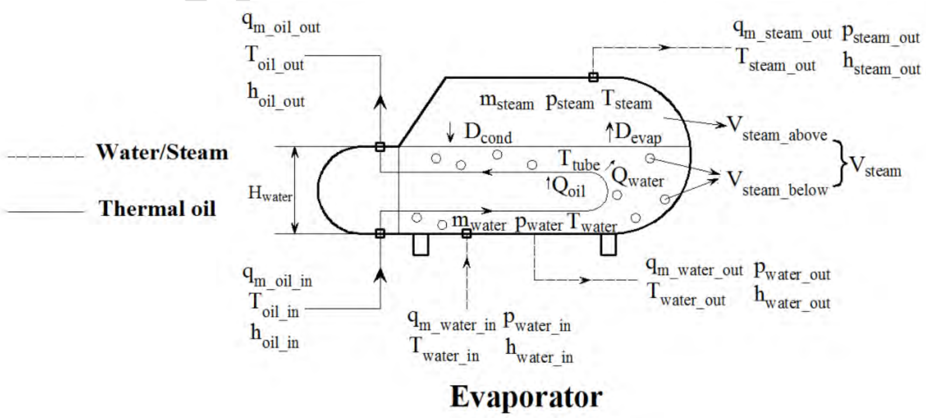

Fig. 6. Schematic diagram of the evaporator model.

To model the water level in the evaporator, the steam volume at the shell side needs to be divided into two parts, the part below the water surface and the other above the water surface, as shown in Fig. 6. In addition, the water dynamic evaporation and the steam dynamic condensation should be considered as well. The model of the water level is expressed as

$$H_{water} = (V_{water} + V_{steam\_below}) / S = (\frac{m_{water}}{\rho_{water}} + V_{steam\_below}) / S , \tag{20}$$

where

$$\frac{dm_{water}}{dt} = q_{m\_water\_in} + q_{m\_cond} - q_{m\_evap} - q_{m\_water\_out} , \tag{20-a}$$

$$V_{steam\_below} = a + bq_{m\_evap} . \tag{20-b}$$

Here, q_{m_evap} denotes the water dynamic evaporation, and q_{m_cond} denotes the steam dynamic condensation, which are calculated by Eq. (21) and Eq. (22) [3]:

$$q_{m\_evap} = \frac{Q_{water} - m_{water}(h_{water} - h^{0}_{water}) / \Delta t}{h_{steam} - h_{water}} , \tag{21}$$

$$q_{m\_cond} = \frac{q_{m\_water\_in}(h_{water} - h_{water\_in})}{h_{steam} - h_{water}} . \tag{22}$$

Eq. (20-b) is given based on the relationship that the variation of the steam volume below the water surface with mass of evaporation is linear [56]. Moreover, analyzing Eq. (20), it can be seen that the water level is determined by three factors, namely, the imbalance of the input and output mass, the pressure in the evaporator, and the steam volume below the water surface.

The energy conservation equation based on the thermodynamics principle at the heat transfer tube wall is expressed as

$$\frac{d(c_{p\_tube} m_{tube} T_{tube})}{dt} = Q_{oil} - Q_{water} . \tag{23}$$

3.2.4 Solution method for the model of the SGS

In this paper, the method adopted to solve the model of the SGS is the implicit Euler method, which is usually used to solve the ordinary differential equation set about *t* [57]. The solution flow chart is shown in Fig. 7.

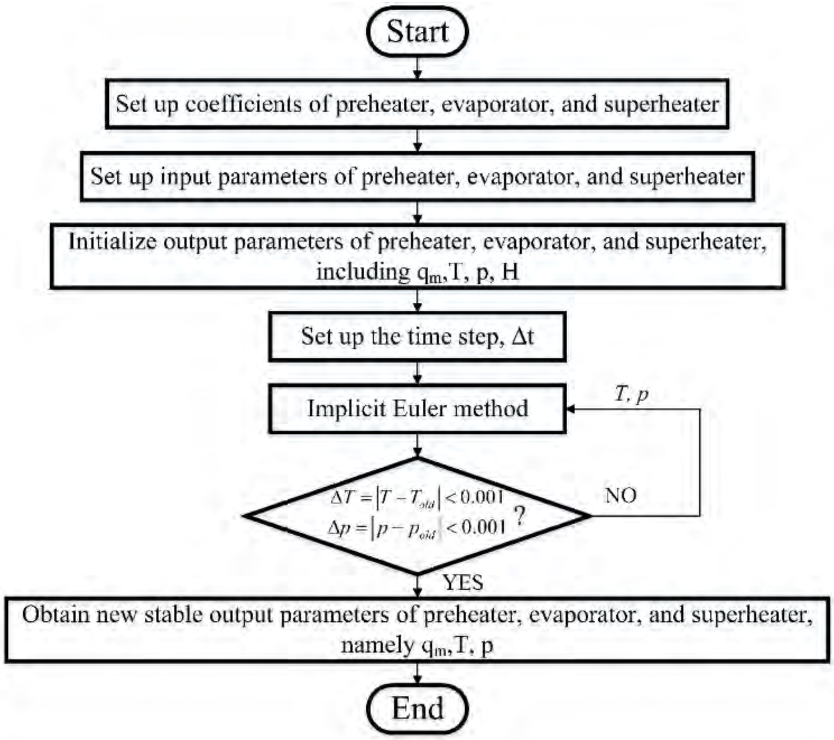

Fig. 7. Solution flow chart.

3.2.5 Model validation

In the field of simulation, one of the criteria for validating a developed model is that the steady-state accuracy of key parameters is within the range of ±2% [58]. Therefore, to validate the accuracy of the SGS model, the steady-state simulation values of key parameters under the rated operation conditions are compared with design values first. The comparison results are shown in Table 2. As seen in Table 2, the simulation values are in good agreement with the design values, and the maximum error is not more than 1%, which meets the accuracy requirement.

TABLE 2. Comparison of design values and simulation values

	Preheater		Evaporator			Superheater	
	Outlet oil temperature	Outlet water temperature	Outlet oil temperature	Outlet steam temperature	Outlet steam pressure	Outlet oil temperature	Outlet steam temperature
Design values	296 °C	230 °C	317.9 °C	235.1 °C	3.12 MPa	379.9 °C	383 °C
Simulation values	296.0 °C	231.7 °C	315.7 °C	236.0 °C	3.12 MPa	379.7 °C	383.4 °C
Relative errors	0%	0.74%	0.69%	0.38%	0%	0.05%	0.10%

4. Dynamic simulations of the SGS and discussions

4.1 Dynamic simulations of single-parameter disturbance

Based on the validated model of the SGS, dynamic simulations of single-parameter disturbance were carried out to study the dynamic characteristics of the SGS when a disturbance occurs and develop a reasonable control strategy for system-level simulations. Four typical disturbance processes, namely disturbance of the feed water mass flow rate and the steam mass flow rate as well as step disturbance of the thermal oil inlet mass flow rate and inlet temperature were simulated.

4.1.1 Dynamic simulations of the feed water mass flow rate disturbance

To adjust the water level in the SGS during operation, it is necessary to increase or decrease the feed water mass flow rate, which can be realized by increasing or decreasing the opening of the feed water valve. Therefore, the processes of increasing and decreasing the opening of the feed water valve by 20% were simulated. At the beginning of the simulations, the SGS works under the rated operation condition. The two simulations both start at t = 0 s. For the simulation of increasing the opening of the feed water valve, when t = 863 s, the opening of the feed water valve increases by 20% and lasts 471 s. For the simulation of decreasing the opening of the feed water valve, when t = 920 s, the opening of the feed water valve decreases by 20% and lasts 414 s. The simulation results are shown in Fig. 8.

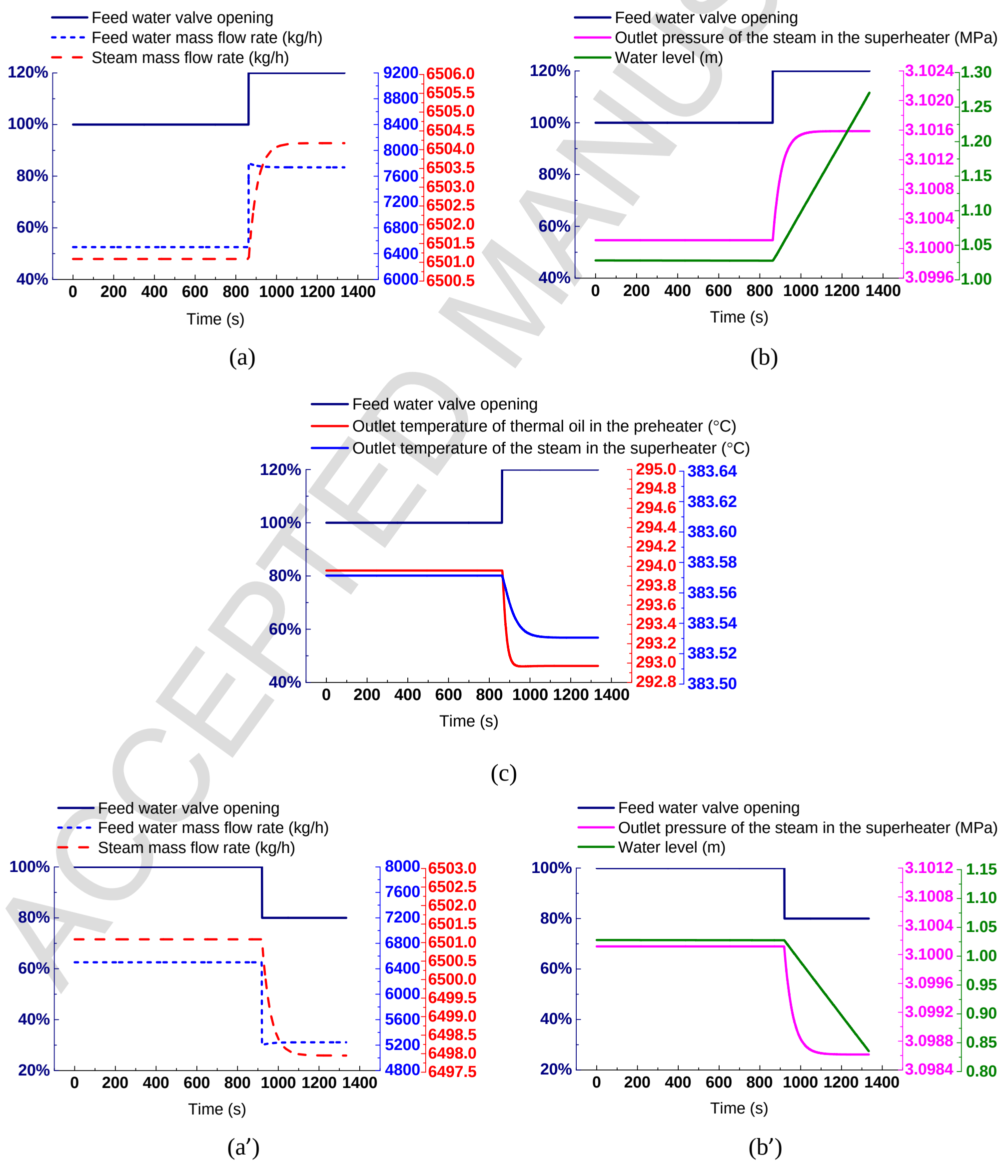

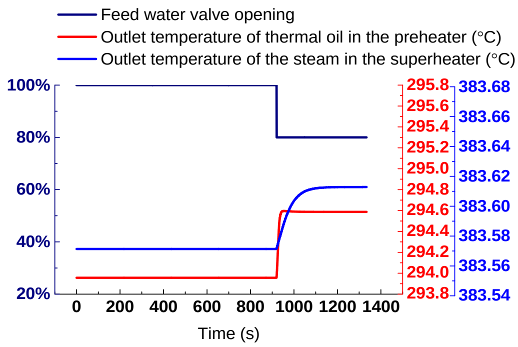

(c′)

Fig. 8. Results of the dynamic simulation of the feed water mass flow rate disturbance.

In the dynamic simulation of increasing the feed water mass flow rate, after the opening of the feed water valve increases by 20%, the feed water mass flow rate steps up from 6500 kg/h to 7802 kg/h immediately. The increase in the feed water mass flow rate enhances convection heat transfer in the preheater, so the thermal oil temperature at the outlet of the preheater decreases, finally reaching 293 °C, which is shown in Fig. 8 (c). Based on the principle of energy conservation, the increase in the feed water mass flow rate leads to a decrease in the feed water temperature at the outlet of the preheater. Hence, the lower enthalpy of the feed water increases. Analyzing the second term in the right numerator of equation (17), the increase in the feed water mass flow rate causes an increase in the steam pressure in the evaporator and the increase in the feed water lower enthalpy leads to a decrease in that. The final effect of these two contrary trends makes the pressure in the evaporator slightly increase. Therefore, the outlet pressure of the superheated steam in the superheater increases gradually to 3.1016 MPa. According to equations (18) and (19), with the increase in the steam pressure, the steam mass flow rate also increases, finally reaching 6504 kg/h, but the feed water mass flow rate decreases, from 7802 kg/h to 7737 kg/h. Therefore, the feed water mass flow rate steps up first and then gradually decreases to a new stable value that is larger than that before the disturbance as shown in Fig. 8 (a). The feed water mass flow rate is always higher than the steam mass flow rate, so the water level in the evaporator increases linearly as shown in Fig. 8 (b). The outlet temperature of the superheated steam in the superheater also decreases, which finally reaches 383.53 °C, because the increase in the steam mass flow rate leads to a decrease in the steam temperature rise based on the principle of energy conservation. The temperature variation mentioned above is shown in Fig. 8 (c). The whole system works under a new stable operation condition after about 200 s.

In the dynamic simulation of decreasing the feed water mass flow rate, after the opening of the feed water valve decreases by 20%, variation trends of the main system parameters are contrary to those in the dynamic simulation of increasing the feed water mass flow rate as shown in Fig. 8 (a′), (b′) and (c′). The variation trends can be explained by causes which are contrary to those given in the former simulation. The whole system works under a new stable operation condition after about 300 s.

4.1.2 Dynamic simulations of the steam mass flow rate disturbance

The power output of the turbine-generator unit in a PTSP plant is often adjusted according to the requirements of the grid load, which can be realized by adjusting the steam mass flow rate into the turbine–generator unit. Thus, the processes of increasing and decreasing the opening of the steam valve by 20% were simulated. At t = 0 s, the SGS runs under the rated operation condition. For the simulation of increasing the opening of the steam valve, when t = 395 s, the opening of the steam valve increases by 20% and remains at this level for 270 s. For the simulation of decreasing the opening of the steam valve, when t = 433 s, the opening of the steam valve decreases by 20% and remains for 317 s. The simulation results are shown in Fig. 9.

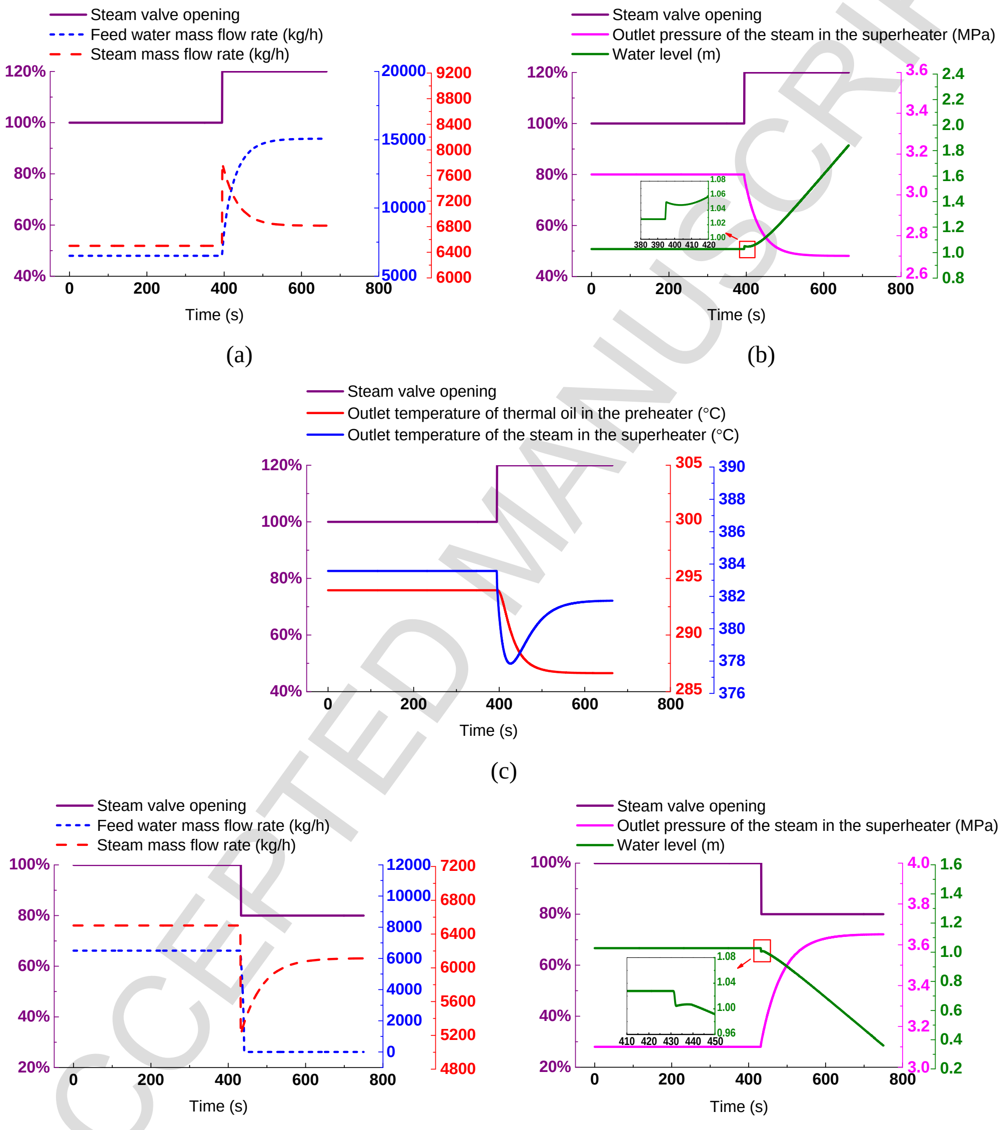

(a) (b)

(c)

(a’) (b’)

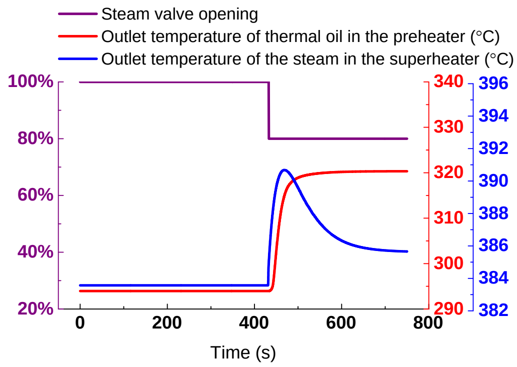

(c′)

Fig. 9. Results of the dynamic simulation of the steam mass flow rate disturbance.

In the dynamic simulation of increasing the steam mass flow rate, after the opening of the steam valve increases by 20%, the steam mass flow rate suddenly increases to 7788 kg/h. With the increase of the mass flow rate of the steam flowing out of the evaporator, the pressure in the evaporator decreases. Therefore, the outlet pressure of the steam in the superheater gradually declines and ultimately reaches 2.73 MPa. With the decrease in the steam pressure, according to equations (18) and (19), the feed water mass flow rate gradually increases, and the steam mass flow rate decreases. Hence, the steam mass flow rate also steps up first and then decreases gradually to a new stable value that is larger than the original value. The variation is similar to that of the feed water mass flow rate in the first disturbance simulation, which is shown in Fig. 9 (a). As seen in Fig. 9 (b), the water level increases overall, but in the first 30 s after the disturbance, the water level rises first and then decreases and gradually increases again, which is called the "false water level" [59]. This is caused by the imbalance of the input and output mass, the pressure in the evaporator, and the steam volume below the water surface. After the opening of the steam valve increases by 20%, the pressure in the evaporator deceases instantly, so the water temperature at this time is higher than the saturation temperature that corresponds to the new pressure. Therefore, some water vaporizes, and the steam volume below the water surface increases, making the water level temporarily rise. When the vaporized steam escapes from the water, the water level falls. Then the water level rises again because the water mass flow rate is higher than the steam mass flow rate in the end. As seen in Fig. 9 (c), after the disturbance, the outlet temperature of the thermal oil in the preheater gradually decreases to 287 °C due to enhanced convection heat transfer in the preheater caused by the increase in the feed water mass flow rate. The outlet temperature of the steam in the superheater declines first and then rises to 382 °C because the steam mass flow rate increases first and then decreases. The new steady-state temperature of the steam is larger than that before the disturbance. The system transition time is also about 200 s.

In the dynamic simulation of decreasing the steam mass flow rate, after the opening of the steam valve decreases by 20%, variation trends of the main system parameters are contrary to those in the former simulation as shown in Fig. 9 (a′), (b′) and (c′). They can be explained by causes which are contrary to those given in the dynamic simulation of increasing the opening of the steam valve by 20%. The whole system works under a new stable operation condition after about 270 s. In addition, the feed water mass flow rate decreases to 0 kg/h finally as shown in Fig. 9 (a′) because the pressure in the evaporator (3.67 MPa) is higher than the feed water pressure (3.21 MPa) under the new stable operation condition.

4.1.3 Dynamic simulation of the thermal oil inlet mass flow rate step disturbance

Because DNI changes over the course of one day, it is usually necessary to regulate the mass flow rate of the thermal oil flowing through the collector field, which is also the mass flow rate of the thermal oil flowing through the SGS, to keep the outlet temperature of the thermal oil in the collector field constant. Therefore, the process of reducing the thermal oil inlet mass flow rate by 10% was simulated. Before the step disturbance starts, the SGS works under the rated operation condition. When t = 347 s, the thermal oil inlet mass flow rate is reduced by 10%, from 74,130 kg/h to 66,717 kg/h, and it lasts 342 s. The simulation results are shown in Fig. 10.

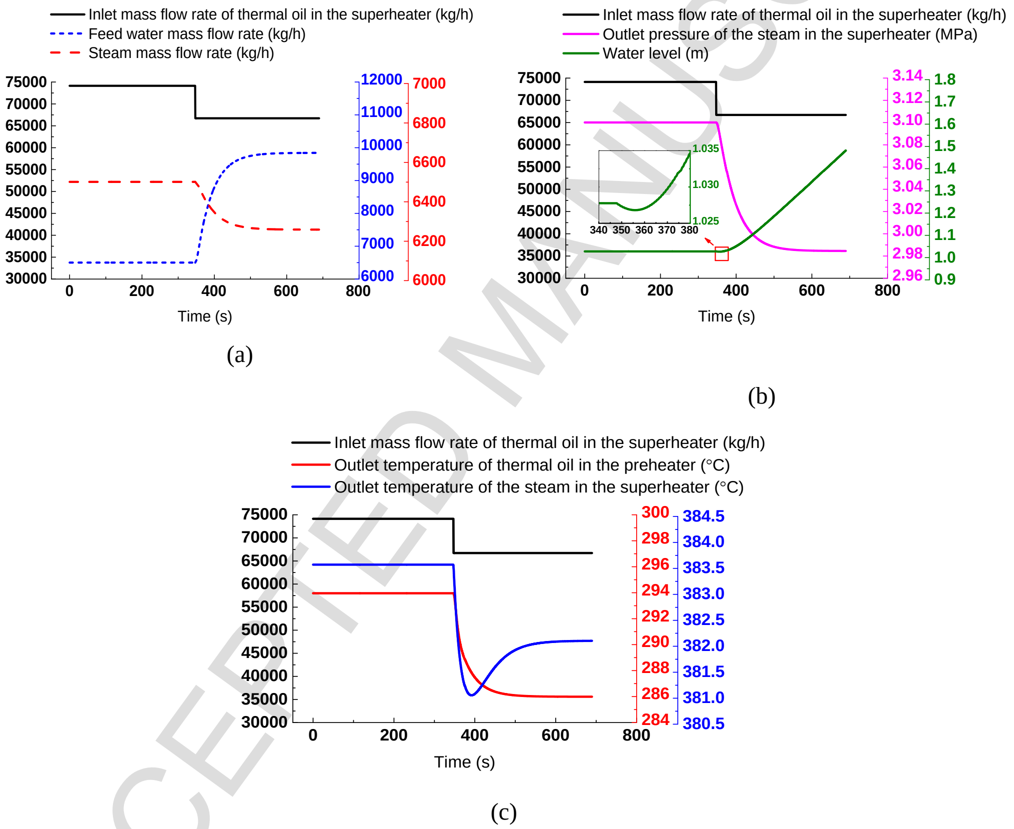

Fig. 10. Results of the dynamic simulation of the thermal oil inlet mass flow rate step disturbance.

In the dynamic simulation of the thermal oil inlet mass flow rate step disturbance, when the thermal oil inlet mass flow rate steps down, convection heat transfer at the thermal oil side in the evaporator weakens. Therefore, the heat released by the thermal oil decreases and the amount of the generated steam also decreases, leading to a decline of the steam pressure in the evaporator. The outlet pressure of the steam begins to drop and finally reaches 2.98 MPa. According to equations (18) and (19), the decrease in the steam pressure leads to an increase in the feed water mass flow rate, which eventually reaches 9842 kg/h. However, the steam mass flow rate falls to 6259 kg/h as shown in Fig. 10 (a). As shown in Fig. 10 (b), in this disturbance process, a “false water level” also occurs. Due to the decrease in the thermal oil inlet mass flow rate, the heat absorbed by the water decreases, and the steam volume below the water surface decreases, so the water level declines. When the underwater steam volume is stable again, the water level increases, which is determined by the imbalance of the input and output mass from then on. Analysis of the variations in the working fluid temperature shown in Fig. 10 (c) reveals that when the thermal oil inlet mass flow rate steps down, the decrease in the thermal oil inlet mass flow rate leads to an increase in the thermal oil temperature drop based on the principle of energy conservation, so the outlet temperature of the thermal oil in the preheater begins to drop until 286 °C. Also, the temperature of the steam at the outlet of the superheater decreases first and then increases to 382.1 °C, which is lower than the temperature before disturbance. The reason for the variation of the steam temperature is that, although the steam mass flow rate decreases with the step down of the thermal oil inlet mass flow rate, the variation is insufficient to eliminate the impact of the decrease of the thermal oil inlet mass flow rate on the outlet steam temperature, so it decreases. When the steam mass flow rate continues to decrease, the outlet steam temperature begins to rise. It takes about 200 s for the system to work under a new steady-state operation condition.

4.1.4 Dynamic simulation of the thermal oil inlet temperature step disturbance

In the process of keeping the outlet temperature of the thermal oil in the collector field constant by adjusting the thermal oil mass flow rate, the outlet temperature, which is also the temperature of the thermal oil entering the SGS, does not remain stable at first due to the thermal inertia of the collectors. Although the step disturbance of the temperature cannot occur during actual operation of the system, the dynamic characteristics in this case are more obvious and can be compared with the results obtained in the process of the thermal oil inlet mass flow rate step disturbance, so the dynamic process of the thermal oil inlet temperature step disturbance was simulated. At the start of the simulation, the SGS works under the rated operation condition. When t = 245 s, the inlet temperature of the thermal oil in the system steps down by 10% from 393 °C to 354 °C, and it lasts for 217 s. The simulation results are shown in Fig. 11.

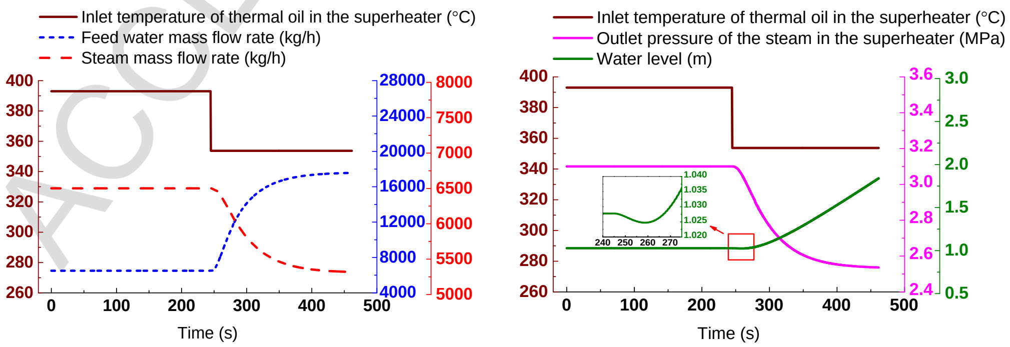

(a) (b)

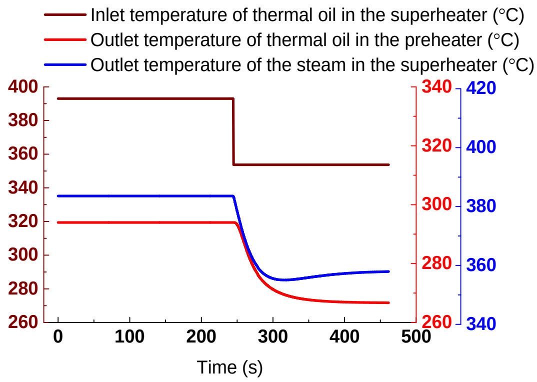

(c)

Fig. 11. Results of the dynamic simulation of the thermal oil inlet temperature step disturbance.

In the dynamic simulation of the thermal oil inlet temperature step disturbance, when the thermal oil inlet temperature steps down, the heat released by the thermal oil in the evaporator decreases and the amount of the generated steam also decreases, leading to a decline of the steam pressure. Hence, the pressure of the steam at the outlet of the superheater begins to decrease and finally reaches 2.53 MPa. As the pressure in the evaporator drops lower, according to equations (18) and (19), the feed water mass flow rate rises and eventually reaches 17,634 kg/h, while the steam mass flow rate decreases, eventually reaching 5309 kg/h as shown in Fig. 11 (a). As seen in Fig. 11 (b), in this case, the "false water level" phenomenon also occurs; the water level decreases first and then increases. The reason is the same as in the process of the thermal oil inlet mass flow rate step disturbance. As seen in Fig.11 (c), when the disturbance occurs, the outlet temperature of the thermal oil in the preheater starts to drop due to the decrease in the thermal oil temperature at the inlet, finally reaching 267 °C. The outlet temperature of the steam in the superheater decreases first and then increases, finally reaching 358 °C, which is lower than the steady-state temperature before the disturbance. The reason for the variation of the steam temperature change is also the same as in the process of the thermal oil inlet mass flow rate step disturbance. The transition time of the entire system is about 200 s.

4.2 System-level simulations

To present the unique dynamic characteristics of the SGS in a PTSP plant, the influence of DNI variation on the output of the SGS should be considered. Therefore, the SGS model was connected with the existing dynamic model of the collector field of the Yanqing 1-MWe PTSP pilot plant developed by Zhao [44, 60], and system-level simulations were conducted on the STAR-90 simulation platform. The collector field model includes a DNI model, a solar collector assembly (SCA) operation model, an SCA optical model, and an absorber model [44, 60, 61]. A schematic diagram of the SGS model connected with the collector field model on the STAR-90 simulation platform is shown in Fig. 12. It should be noted that the STAR-90 simulation platform is a real-time simulation platform, so it will take the platform one year to conduct system-level simulations during an entire year. Hence, in this paper, the simulations are limited to those on different days, including the clear and the cloudy, and on typical days in different seasons.

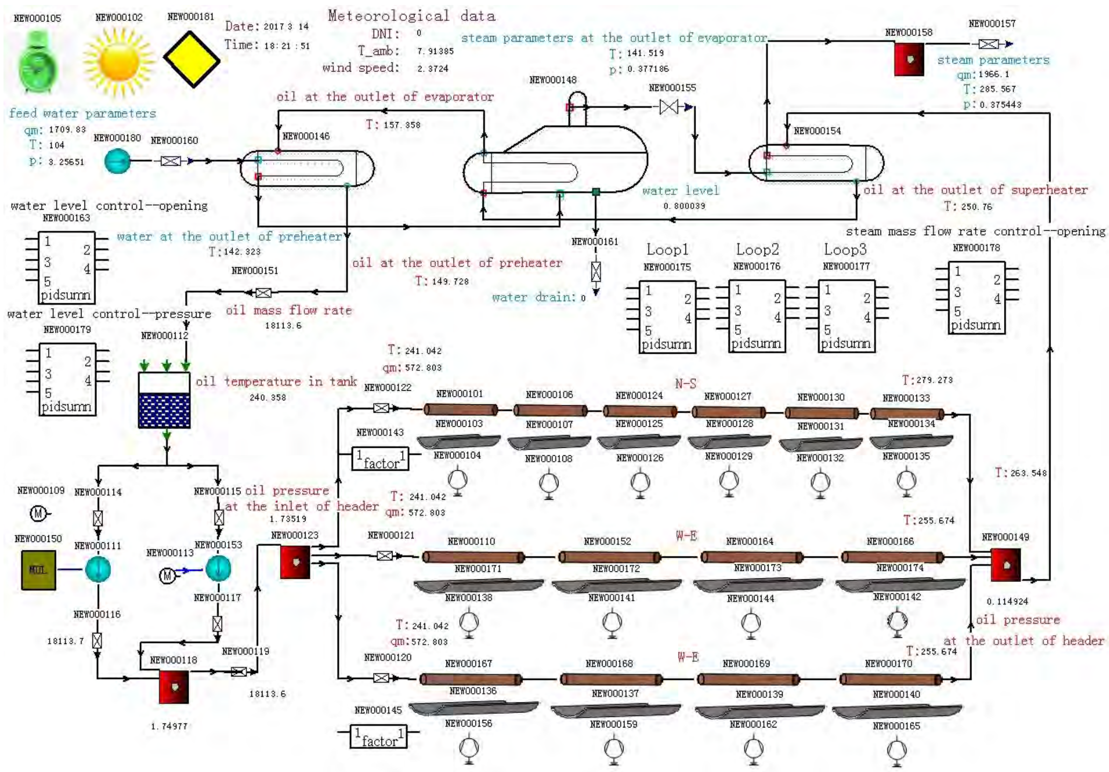

Fig. 12. Schematic diagram of the SGS model connected with the collector field model on the STAR-90 simulation platform.

4.2.1 Control strategy design

To conduct system-level simulations, a reasonable control strategy is required, which can be obtained based on the dynamic simulation results of single-parameter disturbances previously presented.

A comparison of the dynamic simulation results of the feed water mass flow rate disturbance with those of the steam mass flow rate disturbance indicates that the variations of the system parameters, such as working fluid outlet temperature and the steam outlet pressure, are more sensitive to the steam mass flow rate disturbance. In the processes of the feed water mass flow rate disturbances, the variations of the outlet temperature of the thermal oil in the preheater and the steam in the superheater are only 1 °C and 0.04 °C for the process of increasing the opening of the feed water valve, 0.63 °C and 0.04 °C for the process of decreasing the opening of the feed water valve, respectively, and the variations of the steam pressure at the outlet of the superheater are only about 0.0016 MPa (1.6 kPa) and 0.0015 MPa (1.5 kPa), respectively. In addition, no “false water level” phenomena occur because the variations of pressure in the evaporator are small. In the processes of the steam mass flow rate disturbances, the “false water level” is not obvious. The maximum water level fluctuations are only 20 mm and 23 mm, respectively.

Analysis of the results obtained from the dynamic simulations of the thermal oil inlet mass flow rate and temperature step disturbance indicates that the step disturbance of the thermal oil inlet temperature has a more significant influence on the system parameters. In the process of the thermal oil inlet temperature step disturbance, the thermal oil and steam outlet temperature variations are 26 °C and 25 °C, respectively, and the steam outlet pressure variation is 0.57 MPa, which are all larger than those in the process of the thermal oil inlet mass flow rate step disturbance. In addition, the "false water level" occurring in these two processes is also not obvious. The maximum variations are only 1 mm and 3 mm, respectively.

Therefore, to guarantee system parameter stability during operation, the steam mass flow rate, rather than the feed water mass flow rate, is controlled. It is maintained at 6500 kg/h by regulating the opening of the steam valve. And the outlet temperature of the thermal oil in the collector field, that is, the inlet temperature of the thermal oil in the SGS is maintained at 393 °C by regulating the thermal oil mass flow rate, which is the same as the control strategy used in many commercial PTSP plants. Moreover, because the "false water level" is not obvious for the SGS in Yanqing, PI control by regulating the feed water mass flow rate can be adopted for water control [59]. During the simulations, the desired water level was set as 0.8 m, and the mass flow rate of the feed water was regulated by adjusting its pressure and the opening of the feed water valve. A schematic diagram of the control strategy is shown in Fig. 13.

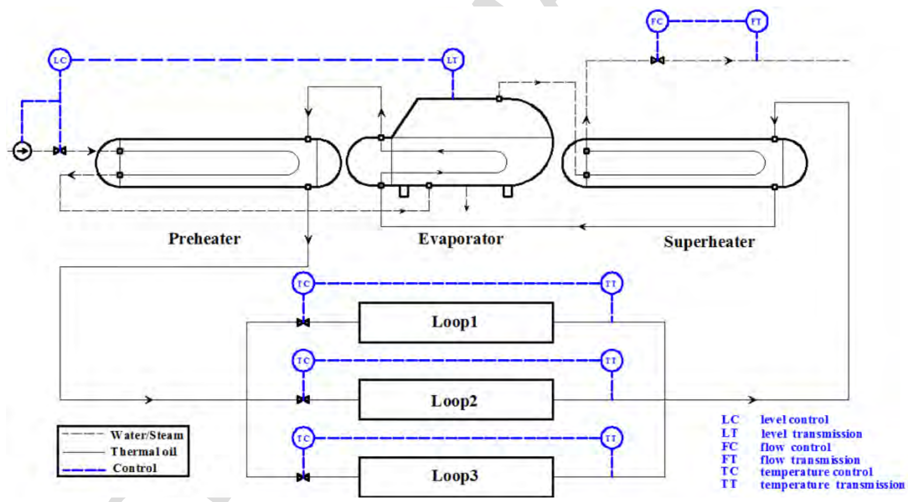

Fig. 13. Schematic diagram of control strategy for system-level simulations.

4.2.2 Boundary conditions

Real meteorological data in Yanqing was selected as boundary conditions for the system-level simulations. The data includes the DNI variations, wind speed, and ambient temperature on different days (clear and cloudy) and in different seasons (spring, summer, autumn, and winter) as shown in Fig. 14.

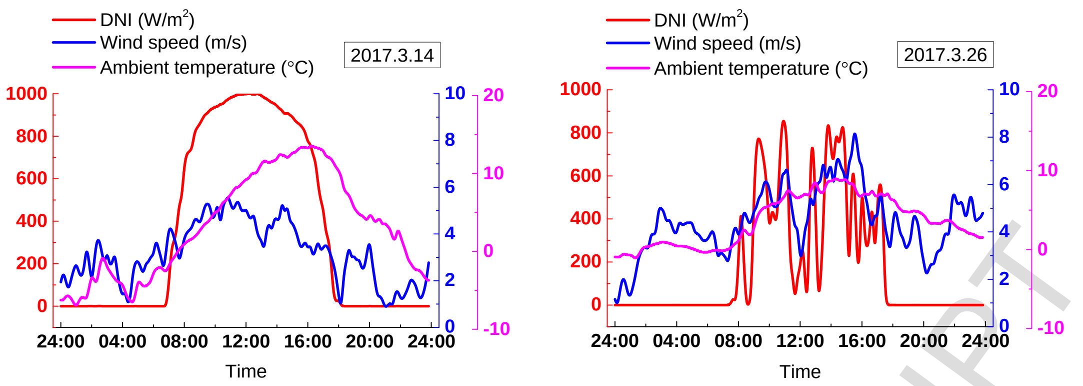

(a) on different days (clear and cloudy)

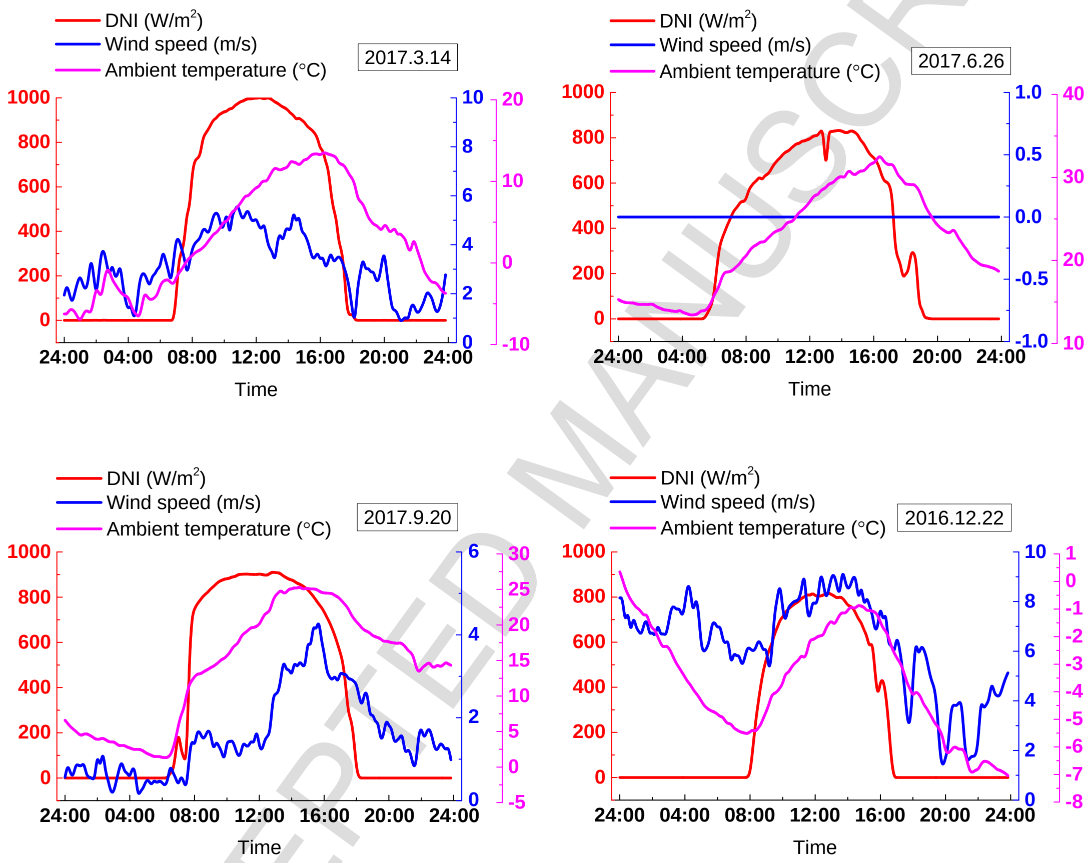

(b) in different seasons (spring, summer, autumn, and winter)

Fig. 14. Real meteorological data in Yanqing.

As seen in Fig. 14 (a), on a clear day, the DNI variation with time is smooth, and DNI reaches its maximum value, 1000.6 W/m^2, at 12:00. By contrast, on a cloudy day, the DNI variation shows oscillation, and its maximum value is only 878.2 W/m^2.

For the real meteorological data in different seasons, some data from typical days, specifically, the spring equinox (March 20th), the summer solstice (June 21st), and the autumn equinox (September 23rd), was not chosen because it was rainy or cloudy on those days. Therefore, the meteorological data of clear days nearest to these typical days was used as shown in Fig. 14 (b). As seen in Fig. 14 (b), DNI reaches its maximum value around 12:00 on each day, but the ambient temperature has its peak value in the afternoon at about 16:00. On June 26th, the sun rises at 5:30 and sets at 19:30, so the duration of sunshine is 14 h. The day length on March 14th is equal to that on September 20th, which is nearly 12 h. On December 22nd, the day length is only 8.5 h. In addition, on June 26th, the value of DNI in Yanqing is not the maximum among the four selected days due to lower atmosphere transparency caused by poor air quality. Fig. 14 (b) also shows that on December 22nd, there is strong wind in Yanqing but lighter breezes on March 14th and September 20th. On June 26th, there is no wind, which causes tiny particles to float in the air and leads to poor air quality.

The meteorological header file was programmed using the real meteorological data on different days and in different seasons and then saved in the STAR-90 algorithm library. The time resolution of the meteorological dataset is 10 min and that of the dynamic simulation code is 0.5s, so in order to match them, the linear interpolation method was adopted during each simulation.

4.2.3 Simulations on different days

Before the simulations on different days started, the initial conditions had to be set first. For comparison, the initial conditions for the simulation on the clear day were the same as that on the cloudy day. The initial temperature of the thermal oil in the collector field was set to 120 °C. The initial mass flow rate and pressure of the steam were set to 0 kg/s and 0.1 MPa, respectively. The initial water level in the evaporator was set to 0.678 m. The temperature of the feed water was set to 104 °C and was maintained during the simulations. The simulation results are shown in Fig. 15.

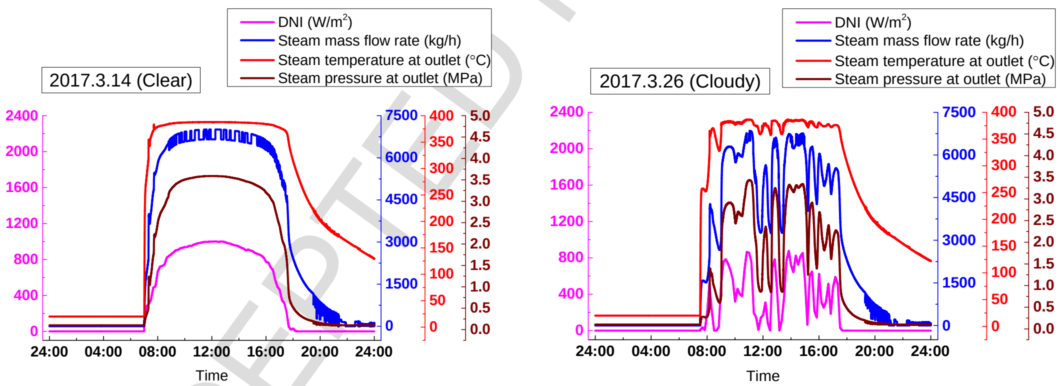

(a)

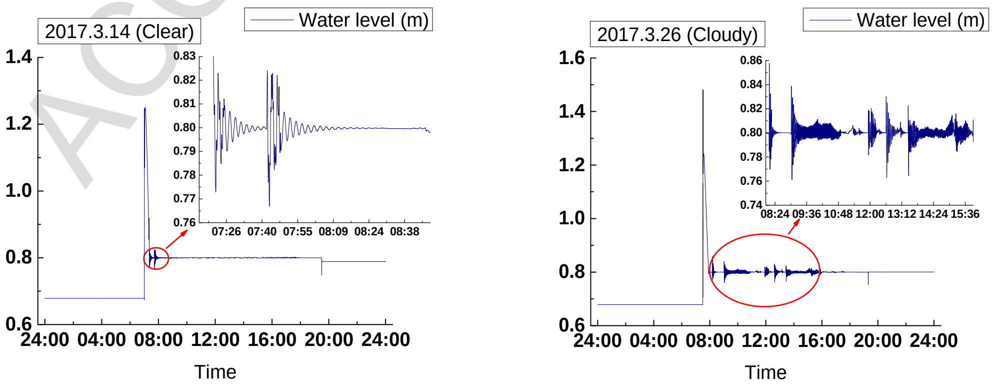

(b)

Fig. 15. Results of system-level simulations on different days (steam mass flow rate, steam temperature, steam pressure, and water level).

As seen in Fig. 15, on the clear day, the steam mass flow rate, temperature, and pressure vary with DNI, and the steam temperature reaches the stable value, about 387 °C, earlier than the other two parameters. The reason is that the amount of the steam generated by SGS is lower at the initial stage of operation when DNI is low, which increases the steam temperature rise rate, and the SGS requires more heat, namely higher DNI, to generate more steam to obtain the stable steam mass flow rate and pressure. Hence, it takes the steam mass flow rate and pressure longer to reach the stable values. At 8:47, the steam mass flow rate starts to oscillate slightly around 6500 kg/h until 16:27 because the control for the steam valve functions. On the cloudy day, the steam mass flow rate, temperature, and pressure also vary with DNI, but they vary more widely than on the clear day due to the drastic variation of DNI on the cloudy day. In addition, the variation of the steam temperature shows inertia in comparison with the variation of the other two parameters due to the thermal storage capacity of the SGS. On the clear day, the water level oscillates at first because the adjustment of the water level by PI control needs transition time. On the cloudy day when DNI varies rapidly, to keep the thermal oil temperature at the outlet of the collector field constant, the mass flow rate of the thermal oil in the collector field, that is, the mass flow rate of the thermal oil flowing into the SGS, oscillates frequently. Thus, the SGS operates with frequent disturbances, and PI control of the water level functions continuously. Therefore, the water level oscillates longer. In addition, the water level is controlled well, and its maximum dynamic deviation is 6 mm (the first peak value of the water level is mainly caused by the initial conditions, not by the control strategy), even under strong disturbance conditions on the cloudy day.

4.2.4 Simulations in different seasons

The initial conditions also had to be set before the simulations for different seasons started. For comparison, the initial conditions for the simulations in different seasons were set to be identical to those on different days. The simulation results are shown in Fig. 16, Fig. 17 and Fig. 18.

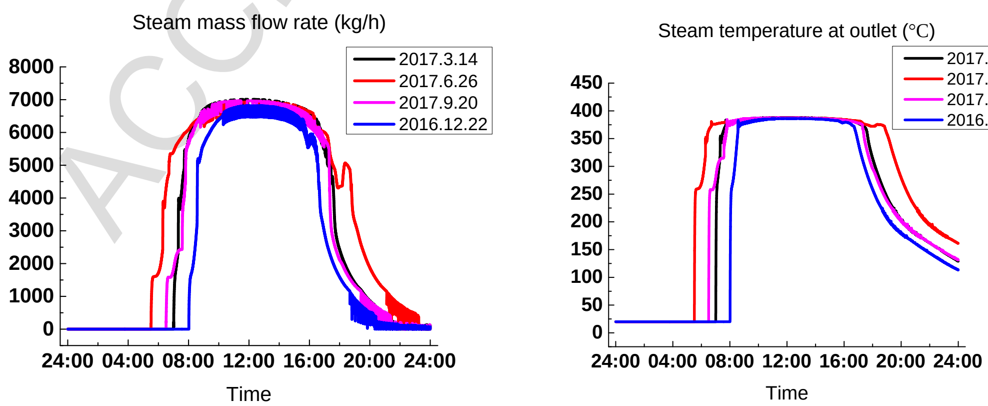

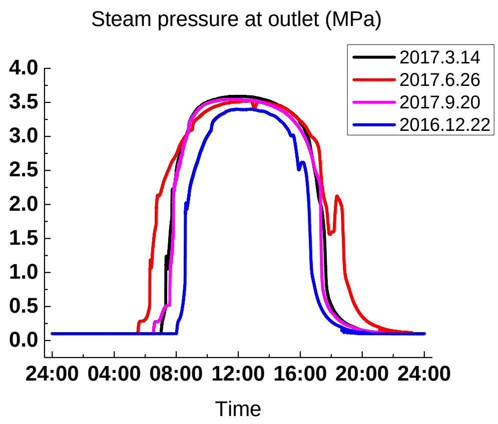

Fig. 16. Results of system-level simulations in different seasons (steam mass flow rate, steam temperature, and steam pressure).

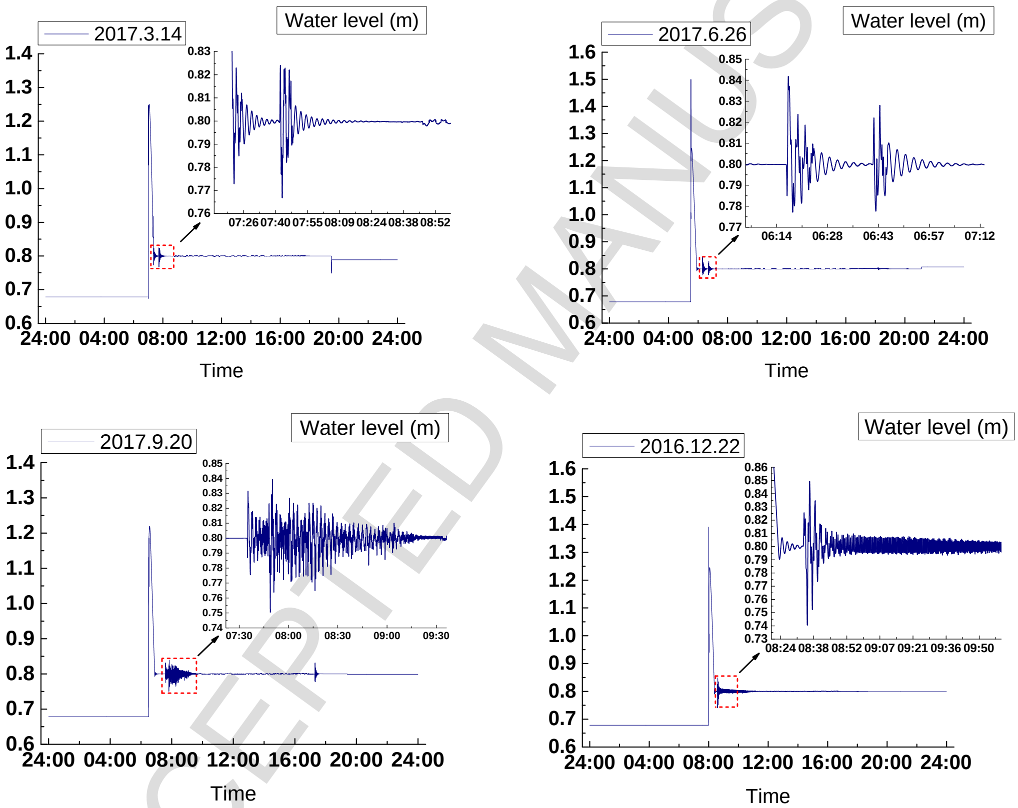

Fig. 17. Results of system-level simulations in different seasons (water level).

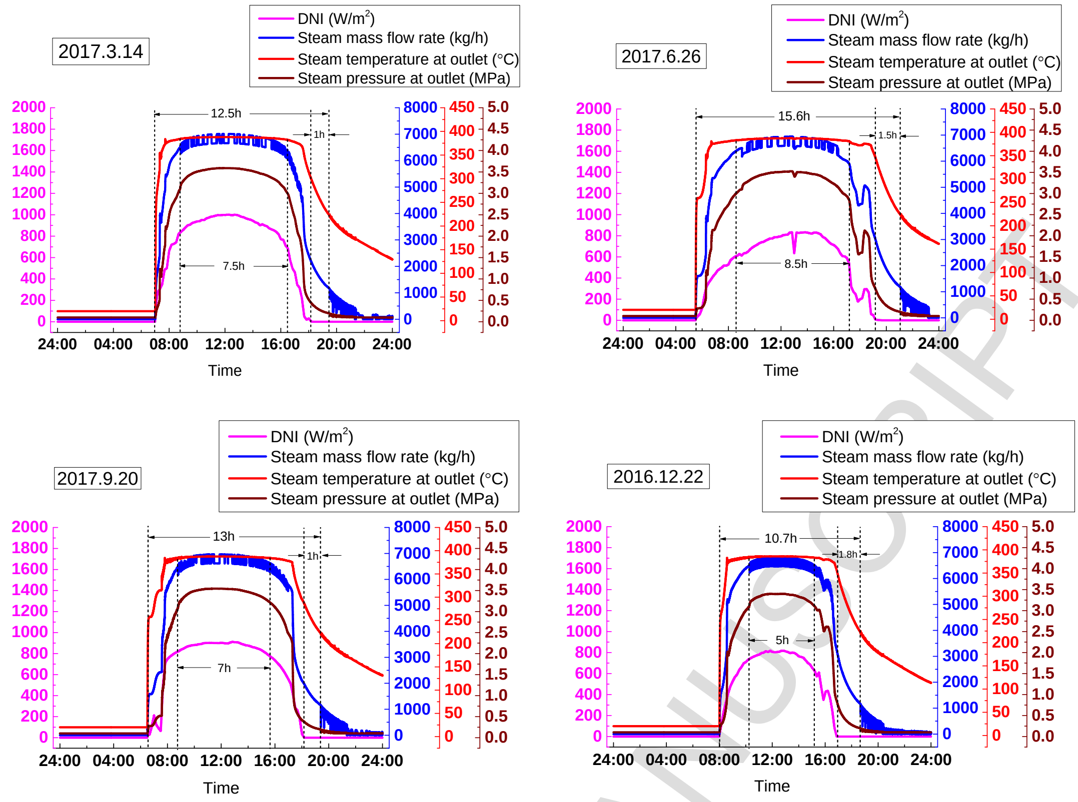

Fig. 18. Results of system-level simulations in different seasons (operation time).

As seen in Fig. 16, on June 26th, the sun rises earliest, so the SGS generates steam first on that day. By regulating the steam valve, the maximum steam mass flow rate is around 6500 kg/h on four days, and the stable temperature the steam reaches is almost the same, about 387 °C, due to thermal storage capacity of the SGS. However, the maximum steam pressure is different on these four days because the maximum DNI is different. On March 14th, the steam pressure is the highest at 3.59 MPa, followed by 3.51 MPa and 3.54 MPa on June 26th and September 20th, respectively. On December 22nd, the maximum pressure the steam can reach is 3.4 MPa, the lowest of the four days. As seen in Fig. 17, the water level oscillates at first in all seasons, and the explanation is the same as that on the clear day. Besides, the water level is controlled well in all seasons, and its maximum dynamic deviation is 6 mm.

In Fig. 18, the stable operation time of the SGS on the four typical days is shown. The stable operation time of the SGS on June 26th is the longest in comparison with the other three selected days, which lasts 8.5 h, followed by 7.5 h, and 7 h on March 14th and September 20th. The time on December 22nd is the shortest, only 5 h. Fig. 18 also shows that the SGS can continue to generate steam after the sun sets because there is still heat stored in the thermal oil in the collector field. The durations are 1 h, 1.5 h, 1 h, and 1.8 h, respectively, on the four days. In addition, Fig. 18 reveals that on June 26th, there is the longest operation time for the SGS in Yanqing in comparison with the other three selected days, which is 15.6 h, followed by 12.5 h and 13 h on March 14th and September 20th, and the time on December 22nd is 10.7 h. The above analysis shows that longer duration of DNI leads to longer operation period of the system.

5. Conclusions and future work

In this paper, the oil/water steam generation system of the Yanqing 1-MWe parabolic trough solar power pilot plant was modeled and the modeling method was presented in detail. In the steady-state validation, the simulation values show good agreement with the design values, and the maximum error is not above 1%. Based on the developed model, four typical single-parameter disturbance and system-level dynamic simulations were carried out. The simulation results provide insights that can be used as guidance for system operation. These insights are summarized as follows.

i. The steam mass flow rate disturbance and the thermal oil inlet temperature step disturbance have more obvious impact on the system parameters. Therefore, the steam mass flow rate and thermal oil inlet temperature should remain unchanged to ensure that the system operates as steadily as possible.

ii. PI control by regulating the feed water mass flow rate can be used to adjust the water level.

iii. The output of the system is greatly influenced by DNI. On a cloudy day, the steam mass flow rate, temperature, and pressure vary with DNI more widely compared to that on a clear day; therefore, system operation on cloudy days should be avoided to guarantee the safety of the steam turbine, or the thermal energy storage system should be used to keep the steam parameters stable. Longer duration of DNI leads to longer operation period, so it can be concluded that in summer, the system has the longest mean operation period in a year.

iv. The plant operators can use this system to continue to generate steam after the sun sets due to the heat stored in the thermal oil in the collector field.

The modeling method described in this paper can also be extended to the modeling of steam generation systems using other working fluid, such as molten salt/water, by changing thermal oil properties to molten salt properties or to properties in a solar thermal power plant with a different capacity, such as 50 MWe. In addition, the developed model is a general model. Thus, it can be used to design simulators of specific PTSP plants together with the corresponding collector field model to train plant operators. In the future, the influence of the DNI will be studied throughout a year by considering a typical meteorological year using other system simulation software. The thermal energy storage system will be considered and its influence on the output and nighttime operation of the SGS will be investigated.

Acknowledgements

This work was supported by the National High Technology Research and Development Program (863 Program) of China: trough collectors, power generation systems experimental platform research and demonstration (2012AA050603); the National Natural Science Foundation of China (51406194).

References

[1] Fritz Zaversky, Marcelino Sánchez, David Astrain. Object-oriented modeling for the transient response simulation of multi-pass shell-and-tube heat exchangers as applied in active indirect thermal energy storage systems for concentrated solar power. Energy 65 (2014): 647-64.

[2] Luis F. González-Portillo, Javier Muñoz-Antón, José M. Martínez-Val. An analytical optimization of thermal energy storage for electricity cost reduction in solar thermal electric plants. Applied Energy 185 (2017): 531-46.

[3] Ershu Xu, Zhifeng Wang, Wei Gao, Jiayan Zhuang. Dynamic simulation of thermal energy storage system of Badaling 1 MW solar power tower plant. Renewable Energy 39 (2012): 455-62.

[4] Kody M. Powell, Khalid Rashid, Kevin Ellingwood, Jake Tuttle, Brian D. Iverson. Hybrid concentrated solar thermal power systems: A review. Renewable and Sustainable Energy Reviews 80 (2017): 215-37.

[5] Qiang Yu, Zhifeng Wang, Ershu Xu. Analysis and improvement of solar flux distribution inside a cavity receiver based on multi-focal points of heliostat field. Applied Energy 136 (2014): 417-30.

[6] Su Guo, Deyou Liu, Xingying Chen, Yinghao Chu, Chang Xu, Qunming Liu et al. Model and control scheme for recirculation mode direct steam generation parabolic trough solar power plants. Applied Energy 202 (2017): 700-14.

[7] Mario Biencinto, Rocío Bayón, Esther Rojas, Lourdes González. Simulation and assessment of operation strategies for solar thermal power plants with a thermocline storage tank. Solar Energy 103 (2014): 456-72.

[8] Z.D. Cheng, Y.L. He, F.Q. Cui, B.C. Du, Z.J. Zheng, Y. Xu. Comparative and sensitive analysis for parabolic trough solar collectors with a detailed Monte Carlo ray-tracing optical model. Applied Energy 115 (2014): 559-72.

[9] Wang Fuqiang, Cheng Ziming, Tan Jianyu, Yuan Yuan, Shuai Yong, Liu Linhua. Progress in concentrated solar power technology with parabolic trough collector system: A comprehensive review. Renewable and Sustainable Energy Reviews 79 (2017): 1314-28.

[10] T.E. Boukelia, M.S. Mecibah, B.N. Kumar, K.S. Reddy. Investigation of solar parabolic trough power plants with and without integrated TES (thermal energy storage) and FBS (fuel backup system) using thermic oil and solar salt. Energy 88 (2015): 292-303.

[11] Flavio Manenti, Zohreh Ravaghi-Ardebili. Dynamic simulation of concentrating solar power plant and two-tanks direct thermal energy storage. Energy 55 (2013): 89-97.

[12] Hongjuan Hou, Junjie Wu, Yongping Yang, Eric Hu, Si Chen. Performance of a solar aided power plant in fuel saving mode. Applied Energy 160 (2015): 873-81.

[13] Guolei Zhang, Yu Zhang, Yuanlong Yang, Yanjun Li, Baozhi Sun. Dynamic heat transfer performance study of steam generator based on distributed parameter method. Annals of Nuclear Energy 63 (2014): 658-64.

[14] P.A. González-Gómez, J. Gómez-Hernández, J.V. Briongos, D. Santana. Transient

thermo-mechanical analysis of steam generators for solar tower plants. Applied Energy 212 (2018): 1051-68.

[15] Z.L. Wang, W.X. Tian, Y.W. Wu, S.Z. Qiu, G.H. Su. Numerical study on annular tube once-through steam generator using compressible flow model. Annals of Nuclear Energy 39 (2012): 49-55.

[16] Jiashuang Wan, Hongbing Song, Shoujun Yan, Jian Sun, Fuyu Zhao. Development of a simulation platform for dynamic simulation and control studies of AP1000 nuclear steam supply system. Annals of Nuclear Energy 85 (2015): 704-16.

[17] Peyman Sindareh-Esfahani, Ehsan Habibi-Siyahposh, Majid Saffar-Avval, Ali Ghaffari, Firooz Bakhtiari-Nejad. Cold start-up condition model for heat recovery steam generators. Applied Thermal Engineering 65 (2014): 502-12.

[18] Peyman Sindareh-Esfahani, Ali Ghaffari, Pouria Ahmadi. Thermodynamic modeling based optimization for thermal systems in heat recovery steam generator during cold start-up operation. Applied Thermal Engineering 69 (2014): 286-96.

[19] Falah Alobaid, Karl Karner, Jörg Belz, Bernd Epple, Hyun-Gee Kim. Numerical and experimental study of a heat recovery steam generator during start-up procedure. Energy 64 (2014): 1057-70.

[20] Nicolas Mertens, Falah Alobaid, Ralf Starkloff, Bernd Epple, Hyun-Gee Kim. Comparative investigation of drum-type and once-through heat recovery steam generator during start-up. Applied Energy 144 (2015): 250-60.

[21] Stefano Bracco, Carlo Cravero. Dynamic simulation of a steam generator for ironing machines. Energy Conversion and Management 84 (2014): 13-9.

[22] Alessandro Biglia, Lorenzo Comba, Enrico Fabrizio, Paolo Gay, Davide Ricauda Aimonino. Steam batch thermal processes in unsteady state conditions: Modelling and application to a case study in the food industry. Applied Thermal Engineering 118 (2017): 638-51.

[23] Yosr Allouche, Szabolcs Varga, Chiheb Bouden, Armando C. Oliveira. Dynamic simulation of an integrated solar-driven ejector based air conditioning system with PCM cold storage. Applied Energy 190 (2017): 600-11.

[24] Asok Ray. Dynamic modelling of once-through subcritical steam generator for solar applications. Applied Mathematical Modelling 4 (1980): 417-23.

[25] R. Ben-Zvi, M. Epstein, A. Segal. Simulation of an integrated steam generator for solar tower. Solar Energy 86 (2012): 578-92.

[26] Jean-Francois P. Pitot de la Beaujardiere, Hanno C.R. Reuter, Sanford A. Klein, Douglas T. Reindl. Impact of HRSG characteristics on open volumetric receiver CSP plant performance. Solar Energy 127 (2016): 159-74.

[27] R. Terdalkar, D. Doupis, M. Clark, A. Joshi and C. Wang. Transient simulation of high temperature high pressure solar tower receiver. Energy Procedia 69 (2015): 1451-60.

[28] Thibault Henrion, Karl Ponweiser, Dirk Band, Thomas Telgen. Dynamic simulation of a solar power plant steam generation system. Simulation Modelling Practice and Theory 33 (2013): 2-17.

[29] Carolina V. Ponce, Doris Sáez, Carlos Bordons, Alfredo Núñez. Dynamic simulator and model predictive control of an integrated solar combined cycle plant.

Energy 109 (2016): 974-86.

[30] B. El Hefni and R. Soler. Dynamic multi-configuration model of a 145 MWe concentrated solar power plant with the ThermoSysPro library (tower receiver, molten salt storage and steam generator). Energy Procedia 69 (2015): 1249-58.

[31] Heiko Schenk, Jürgen Dersch, Tobias Hirsch, Thomas Polklas. Transient simulation of the power block in a parabolic trough power plant. Proceedings of the 11th International Modelica Conference (2015): 605-14.

[32] Wisam Abed Kattea Al-Maliki, Falah Alobaid, Vitali Kez, Bernd Epple. Modelling and dynamic simulation of a parabolic trough power plant. Journal of Process Control 39 (2016): 123-38.

[33] Wisam Abed Kattea Al-Maliki, Falah Alobaid, Ralf Starkloff, Vitali Kez, Bernd Epple. Investigation on the dynamic behaviour of a parabolic trough power plant during strongly cloudy days. Applied Thermal Engineering 99 (2016): 114-32.

[34] David H. Lobón, Loreto Valenzuela, Emilio Baglietto. Modeling the dynamics of the multiphase fluid in the parabolic-trough solar steam generating systems. Energy Conversion and Management 78 (2014): 393-404.

[35] Suvi Suojanen, Elina Hakkarainen, Matti Tähtinen, Teemu Sihvonen. Modeling and analysis of process configurations for hybrid concentrated solar power and conventional steam power plants. Energy Conversion and Management 134 (2017): 327-39.

[36] Leonardo Pelagottia, Kim Sørensen, Thomas J. Condra, Alessandro Franco. Modelling of a coil steam generator for CSP applications. Proceedings from the 55th Conference on Simulation and Modelling (SIMS 55) (2014): 175-83.

[37] Antonio Rovira, Rubén Barbero, María José Montes, Rubén Abbas, Fernando Varela. Analysis and comparison of integrated solar combined cycles using parabolic troughs and linear Fresnel reflectors as concentrating systems. Applied Energy 162 (2016): 990-1000.

[38] P.A. González-Gómez, F. Petrakopoulou, J.V. Briongos, D. Santana. Cost-based design optimization of the heat exchangers in a parabolic trough power plant. Energy 123 (2017): 314-25.

[39] P.A. González-Gómez, J. Gómez-Hernández, J.V. Briongos, D. Santana. Thermo-economic optimization of molten salt steam generators. Energy Conversion and Management 146 (2017): 228-43.

[40] A. Pizzolato, F. Donato, V. Verda, M. Santarelli, A. Sciacovelli. CSP plants with thermocline thermal energy storage and integrated steam generator-Techno-economic modeling and design optimization. Energy 139 (2017): 231-46.

[41] Yibo Yuan, Jing Ding, Jianfeng Lu, Jianping Yang. Thermal performances of heat conducting oil steam generator. Energy Procedia 75 (2015): 3284-9.

[42] Yibo Yuan, Canming He, Jianfeng Lu, Jing Ding. Thermal performances of molten salt steam generator. Applied Thermal Engineering 105 (2016): 163–9.

[43] Canming He, Jianfeng Lu, Jing Ding, Weilong Wang, Yibo Yuan. Heat transfer and thermal performance of two-stage molten salt steam generation system. Applied Energy 204 (2017): 1231-9.

[44] Dongming Zhao, Zhifeng Wang, Ershu Xu, Lingzhi Zhu, Dongqiang Lei, Li Xu et

al. Yanqing solar field: Dynamic optical model and operational safety analysis. Applied Thermal Engineering 110 (2017): 275-89.

[45] D. D. Nation, P. J. Heggs, D. W. Dixon-Hardy. Modelling and simulation of a novel electrical energy storage (EES) receiver for solar parabolic trough collector (PTC) power plants. Applied Energy 195 (2017): 950-73.

[46] Ershu Xu, Qiang Yu, Zhifeng Wang, Chenyao Yang. Modeling and simulation of 1 MW DAHAN solar thermal power tower plant. Renewable Energy 36 (2011): 848-57.

[47] Qiang Yu, Zhifeng Wang, Ershu Xu, Xin Li, Minghuan Guo. Modeling and dynamic simulation of the collector and receiver system of 1 MWe DAHAN solar thermal power tower plant. Renewable Energy 43 (2012): 18-29.

[48] Qiang Yu, Zhifeng Wang, Ershu Xu. Simulation and analysis of the central cavity receiver’s performance of solar thermal power tower plant. Solar Energy 86 (2012): 164-74.

[49] Qiang Yu, Zhifeng Wang, Ershu Xu, Hongli Zhang, Zhenwu Lu, Xiudong Wei. Modeling and simulation of 1 MWe solar tower plant’s solar flux distribution on the central cavity receiver. Simulation Modelling Practice and Theory 29 (2012): 123–36.

[50] Xiaolei Li, Ershu Xu, Shuang Song, Xiangyan Wang, Guofeng Yuan. Dynamic simulation of two-tank indirect thermal energy storage system with molten salt. Renewable Energy 113 (2017): 1311-9.

[51] Solutia. Therminol VP-1 heat transfer fluid-Vapour and Liquid phases. Technical bulletin 7239115C (2008):3.

[52] Wagner W, Kretzschmar H. International steam tables - properties of water and steam on the industrial formulation IAPWS-IF97. Berlin: Springer; 2008.

[53] Weidao Shen, Jungeng Tong. Engineering Thermodynamics. 4th ed. Beijing: Higher Education Press, 2007.

[54] Shiming Yang, Wenquan Tao. Heat Transfer. 4th ed. Beijing: Higher Education Press, 2006.

[55] Meizhong Shi, Zhongzheng Wang. Principle and design of heat exchangers. 5th ed. Nanjing: Southeast University Press, 2014.

[56] Chenyue Zhang. Dynamic characteristics of the boiler and its mathematical models. Beijing: Water Conservancy and Electric Power Press, 1987.

[57] Timothy Sauer. Numerical Analysis. 2nd ed. Boston: Pearson Education Inc., 2013.

[58] Shilin Tang. Computer simulation technology for power plants. Beijing: Science Press, 1996: 14.

[59] Jianguo Wang, Lingfang Sun, Lihui Zhang. Automatic control of the thermal processes in power plants. 2nd ed. Beijing: China Electric Power Press, 2015.

[60] Dongming Zhao. Modeling and dynamic characteristics of the concentrating collector system for the 1MW parabolic trough solar thermal power plant in Yanqing, Beijing. Beijing: National Science Library, Chinese Academy of Sciences (2017): 110-21.

[61] Dongming Zhao, Ershu Xu, Zhifeng Wang, Qiang Yu, Li Xu, Lingzhi Zhu. Influences of installation and tracking errors on the optical performance of a solar

parabolic trough collector. Renewable Energy 94 (2016): 197-212.

Highlights:

1. The modeling method of a steam generation system is provided in detail.
2. System-level simulations are conducted using the real meteorological data.
3. The influence of DNI on the output of the system is analyzed.
4. The steam generation system can continue to generate steam after the sun sets.